JM PAPERS

Amplitude modulation in particle-laden atmospheric surface layers

Hongyou Liu[1], Xibo He[1] and Xiaojing Zheng[2],†

[1]Center for Particle-laden Turbulence, Lanzhou University, Lanzhou 730000, PR China
[2]Research Center for Applied Mechanics, Xidian University, Xi'an 710071, PR China

Particle effects on the amplitude modulation are investigated in this study based on observational data with various mass loading acquired from long-term measurements of aeolian sandstorms in high-Reynolds-number ($Re_\tau \sim O(10^6)$) near-neutral atmospheric surface layers. In both particle-laden and unladen flows, in addition to the positive top–down modulation behaviour in the logarithmic region, a significant modulation effect that exists for some specific motions is also found for the single-point amplitude modulation. The most energetic turbulent motions exhibit the strongest modulation effect, and the modulating signals do not change with the small-scale motions being modulated. In particle-laden flows, the length of the most energetic structure is almost constant, thus the scales of the modulating signal and carrier signal are hardly affected by particles. However, the addition of particles changes the distribution of energy between multi-scale turbulent motions. The kinetic energy of the large-scale component is less enhanced than the total kinetic energy by particles. This leads to a reduced energy proportion of the large-scale component and an augmented one of the small-scale component. Moreover, the particles produce a large damping in the degree of the amplitude modulation and move down the positions of the modulating signals and carrier signals corresponding to the strongest inter-layer modulation, but the damping is weakened with the wall-normal distance due to the decreased mass loading. This study may provide a more general insight into the modulation mechanism between multi-scale turbulent motions and the effect of particles on turbulence.

Key words: atmospheric flows, particle/fluid flow, turbulent boundary layers

1. Introduction

In the 1950s, researchers noticed that there is a series of organized motions, i.e. coherent structures, in random and complex turbulence signals (Dennis 2015). These coherent

† Email address for correspondence: xjzheng@lzu.edu.cn

structures are responsible for the production and dissipation of wall-bounded turbulence and are crucial to understanding the turbulence dynamics (Robinson 1991). Generally, the main coherent structures include the inner streaks associated with the near-wall cycle, hairpin/horseshoe vortices, large-scale motions (LSMs) and very-large-scale motions (VLSMs) or 'superstructures' (Hutchins & Marusic 2007*a*; Marusic *et al.* 2010*a*). In addition to the different wall-normal locations of these coherent structures in the wall turbulence, the difference in scale is more obvious. The hairpin/horseshoe vortex is one of the earliest descriptions of important elementary coherent structures (Theodorsen 1952) with a streamwise length scale of $O(100\nu/U_\tau)$ (Head & Bandyopadhyay 1981), where ν and U_τ denote the kinematic viscosity of the fluid and the friction velocity, respectively. Low-speed streaks are created and maintained by the remnants of the hairpin legs remaining near the wall, which may be stretched into quasi-streamwise vortices (Smith 1984). The streamwise scale of a low-speed streak is approximately $1000\nu/U_\tau$ (Kline *et al.* 1967). The LSMs with a streamwise scale of $\sim 3\delta$ (δ denotes the boundary layer thickness) are created by hairpin vortices aligning coherently in the streamwise direction (hairpin vortex packet), and packets may also align with other packets to create spanwise meandering VLSMs with scales of $\sim 6\delta$ (Kim & Adrian 1999; Adrian, Meinhart & Tomkins 2000; Hutchins & Marusic 2007*a*). In the outer region of the wall turbulence, LSMs and VLSMs have received extensive attention because they are significantly energetic (Guala, Hommema & Adrian 2006; Balakumar & Adrian 2007; Wang & Zheng 2016). Researchers found that these outer large structures have a significant amplitude modulation effect on near-wall small-scale motions (Brown & Thomas 1977; Rajagopalan & Antonia 1980); that is, the amplitudes of the small scales were larger within large-scale positive fluctuations, whereas the small scales became relatively quiescent within large-scale negative fluctuations (Hutchins & Marusic 2007*b*). The phenomenon of amplitude modulation not only contributes to a better understanding of the near-wall turbulence production mechanism (not completely 'self-sustaining' as suggested by Jiménez & Pinelli 1999; Schoppa & Hussain 2002), but also provides an effective way to predict the behaviour of near-wall turbulent motion (Marusic, Mathis & Hutchins 2010*b*; Mathis, Hutchins & Marusic 2011; Mathis *et al.* 2013).

The phenomenon of amplitude modulation was originally studied by Brown & Thomas (1977) and Bandyopadhyay & Hussain (1984) and is highlighted by Hutchins & Marusic (2007*b*). Subsequently, a mathematical tool was proposed by Mathis, Hutchins & Marusic (2009*a*) to quantify the degree of the amplitude modulation, defined as the amplitude modulation coefficient (denoted by R_{AM}). Mathis *et al.* (2009*a*) suggested that the single-point amplitude modulation coefficient provides a reasonable estimate of the degree of modulation by comparing the results of single-point and two-point analyses. Therefore, using high-Reynolds-number boundary layer wind tunnel ($Re_\tau = 2800$–19 000), pipe ($Re_\tau = 3015$), channel ($Re_\tau = 3005$) and atmospheric surface layer (ASL, $Re_\tau = 6.5 \times 10^5$) experimental data (where $Re_\tau = \delta U_\tau/\nu$ is the friction Reynolds number or Kármán number), Mathis *et al.* (2009*a,b*) investigated the single-point R_{AM}. Results indicates that R_{AM} exhibits almost no difference in the internal and external wall-bounded flows but shows a high degree of Reynolds number and wall-normal distance dependence. The value of R_{AM} increased log-linearly with the Reynolds number between the viscous and logarithmic regions ($20 < z^+ < 100$). Based on these studies of the amplitude modulation, Marusic *et al.* (2010*b*) and Mathis *et al.* (2011) proposed a near-wall fluctuating streamwise velocity predictive model. Similarly, Marusic, Mathis & Hutchins (2011), Inoue *et al.* (2012) and Mathis *et al.* (2013) presented a fluctuating wall-shear-stress predictive model. The proposal of these novel near-wall models further highlights the

importance of the amplitude modulation effect. Therefore, there has been continuously increasing interest in exploring amplitude modulation.

The direct numerical simulation (DNS) at $205 < Re_\tau < 1116$ in Bernardini & Pirozzoli (2011) suggested that the genuine top–down interaction can be better captured by exploiting the covariance of the outer large-scale motions and the envelope of the inner small-scale motions. Talluru *et al.* (2014) calculated the amplitude modulation coefficient of large-scale streamwise velocity fluctuations on all three components of the small-scale velocity with measurements from cross-wire probes in the turbulent boundary layer (TBL) at $Re_\tau = 15\,000$ and found that the modulation of the small-scale energy by large-scale structures is relatively uniform across all three velocity components. Luhar, Sharma & McKeon (2014) and Tsuji, Marusic & Johansson (2016) investigated the amplitude modulation of pressure fluctuations and found a relatively small modulation effect between the large- and small-scale components. Squire *et al.* (2016) and Pathikonda & Christensen (2017) explored the inner–outer interactions in rough-wall TBL flows and suggested that the rough wall increases the amplitude modulation coefficient (as well as the numerical simulations results in Nadeem *et al.* 2015; Anderson 2016). Recently, the investigation of the amplitude modulation by DNS of turbulent channel flows in Yao, Huang & Xu (2018) indicated that extraordinary high fluctuation events are provoked by the modulation effect. Salesky & Anderson (2018) present evidence of amplitude modulation phenomena in the unstably stratified (i.e. convective) ASL by a large eddy simulation. They suggested that the modulation by the large-scale streamwise velocity decreases monotonically, while the modulating influence of the large-scale vertical velocity remains significant since the spatial attributes of the flow structures change from streamwise to vertically dominated. The decoupling procedure to calculate the amplitude modulation coefficient employs a nominal cutoff wavelength to divide the fluctuating velocity into large- and small-scale components. The cutoff wavelength (denoted by λ_c) is usually adopted as the boundary layer thickness, i.e. $\lambda_c = \delta$. Much less is known about which scales of motion dominate the amplitude modulation and which scales are significantly subject to the modulation effect. Therefore, Liu, Wang & Zheng (2019) investigated the amplitude modulation between multi-scale turbulent motions using high-Reynolds-number ($Re_\tau \sim O(10^6)$) experimental data in the ASL. They found that the amplitude modulation effect may exist in specific motions rather than at all length scales of motion and proposed an alternative method of decoupling procedure to accurately extract the modulating signals and carrier signals. Recently, Wang & Gao (2021) studied the amplitude and frequency modulation of the outer LSMs onto the inner small-scale motions in turbulent channel flows at $Re_\tau = 550$–1000 and found that the near-wall Reynolds shear stress is easily modulated by the LSMs.

In particle-laden two-phase flows, not only turbulence plays a crucial role in particle transport and aggregation (Toschi & Bodenschatz 2009), but particles also have a significant effect on turbulent motions at different scales, where interest is focused on the effect of the particles on near-wall coherent structures, including near-wall streaks and quasi-streamwise vortices. For example, without considering the gravity of particles, two-way coupled DNS indicated that the particles produce a large damping in the intensity of the streamwise vortices without any significant change in their shape and size, and this damping leads to a weakening of the near-wall streaks (Portela & Oliemans 2003; Zhao, Andersson & Gillissen 2010). The velocity autocorrelations provided in Picano, Breugem & Brandt (2015) showed streamwise elongated structures twice as wide as in single-phase channel flows and a progressive increase of the separation distance with the particle volume fraction. By a DNS of particle-laden turbulence in spatially developing TBL, Li, Luo & Fan (2016) found that with increasing particle mass fraction ($\Phi_m = 0.1$ to 1), small particles ($St = 10$) reduce the streak spacing, while the larger ones with a larger

957 A14-3

Stokes number ($St = 50$) widen it. When the gravity is perpendicular to the flow direction, the experimental study in a horizontal channel by Li *et al.* (2012) suggested that there is no obvious change in the inclination angle of the quasi-streamwise vortex, while the DNS results in Kidanemariam *et al.* (2013) indicated a slightly larger correlation length of the fluid velocity field in the near-wall region where the bulk of the particles is located. In cases of the effect of gravity aligning with the flow, a particle-laden vertical downward channel flow DNS in Li *et al.* (2001) showed that the particles tend to increase the characteristic length scales of the near-wall streaks; Dritselis & Vlachos (2008) indicated that the addition of particles results in a larger diameter and longer streamwise extent of the elongated quasi-streamwise vortices, which in turn reduces the streamwise vorticity of this structure; and Dritselis & Vlachos (2011) suggested a reduction in the inclination angle. It is seen from the existing studies that the effect of the particles on the near-wall coherent structures varies due to many factors, such as particle parameters (including the Stokes number, volume/mass fraction, particle Reynolds number and the ratio of particle size to turbulent characteristic scales), flow conditions (including flow types and Reynolds number) and the configuration of the particle gravity. The stochastic turbulent flow and the distribution of the particle phase make the experiment and numerical simulation of turbulent multi-phase flow more complex than that in single-phase flow (Balachandar & Eaton 2010). Thus, the current understanding of the effect of particles on near-wall structures is far from reaching consensus.

Relatively few studies refer to the effect of the particles on the LSMs/VLSMs, except for Tay, Kuhn & Tachie (2015) and Wang & Richter (2019). Experiments conducted in a water channel with a particle-to-fluid density ratio of approximately 1.19 by Tay *et al.* (2015) suggested that the LSMs are much larger in the particle-laden flow than in the unladen flow, with signs that the inclination angle is slightly larger. Wang & Richter (2019) conducted a two-way coupled DNS with inertial particles (gravitational settling is not considered) to investigate the particle effects on VLSMs. These co-workers found that both low-inertia and high-inertia particles strengthen the VLSMs, whereas the moderate- and very-high-inertia ones have little influence. The particle effects on the near-wall coherent structures are different from those on the LSMs/VLSMs.

In summary, particles have a major impact on the dynamics of the two phases, often triggering turbulent modulation (Mathai, Lohse & Sun 2020). Moreover, the particle effects on coherent structures with different scales also exhibit significant differences. This may change the interaction between multi-scale turbulent motions and then affect the amplitude modulation. However, there is no relevant report yet. Accurately estimating the degree of amplitude modulation is a prerequisite for predictive models of near-wall turbulent motions (Marusic *et al.* 2010*b*; Mathis *et al.* 2011, 2013). Moreover, developing numerical models that correctly represent two-phase flows is responsible for the accurate simulation of the turbulence and particle motion behaviour in the two-phase flow. Therefore, the present work aims to investigate the particle effect on amplitude modulation based on high-Reynolds-number particle-laden two-phase flow experimental data obtained from long-term observations of aeolian sandstorms in the ASL, which is an important environmental flow.

This paper is organized as follows. Section 2 introduces the ASL experimental data acquired at the Qingtu Lake observation array (QLOA) site, including the experimental set-up, data pre-processing, related two-phase flow parameters and the basic flow statistics. Section 3 presents the particle effects on the kinetic energy distribution in large- and small-scale turbulent motions. Given the change in the distribution of turbulent kinetic energy in the particle-laden flow, it is logical then to consider the effect of the particles on

the amplitude modulation of LSMs onto small scales. Therefore, § 4 gives the amplitude modulation covariance to highlight the absolute importance of the modulation effect in particle-laden flows, while the normalized value is provided in § 5 to explore the degree of amplitude modulation with the modulating signals and the carrier signals residing at different flow layers and between multi-scale turbulent motions. Finally, the conclusions from this study are summarized in § 6.

2. Experimental data

2.1. *Experimental set-up*

The high-Reynolds-number particle-laden two-phase flow data are obtained from long-term observations of aeolian sandstorms in ASLs performed at the QLOA site in western China. The QLOA shown in figure 1(*a*) was established on the flat dry lakebed of Qingtu Lake located between the Tenger Desert and the Badain Jaran Desert. The strong northwest monsoons and aeolian sandstorms moving southward pass by this area in the spring, which provides favourable conditions for observations. The QLOA consists of streamwise, spanwise and wall-normal arrays and thus can perform synchronous multi-point measurements of the three-dimensional turbulent flow field for both particle-laden and particle-free flows. More details regarding the experimental set-up at the QLOA site can be found in Wang & Zheng (2016). The fluctuating velocity signals and sand concentration data employed in the present work were derived from the wall-normal array consisting of 11 pairs of velocity and sand concentration probes spaced logarithmically from $z = 0.9$ to 30 m (where z denotes the wall-normal distance). Each pair of velocity and sand concentration probes was placed at the same height, as shown by the schematic in figure 1(*b*). The three components of the wind velocity and the temperature were measured by sonic anemometers (Campbell CSAT3B) with a sampling frequency of 50 Hz. Different from optical measurement methods such as particle image velocimetry, which is a huge challenge in multi-phase flow measurements that typically require optical method and particle size discrimination (Matinpour *et al.* 2019; Petersen, Baker & Coletti 2019), the sonic anemometer estimates the velocity based on the time difference method (Horst & Oncley 2006), without effects from scattered signals by aerosols and, in this case, sand particles. Therefore, the sonic anemometer is widely used to measure the particle-laden flow in the ASL (Li 2013). The sand concentration was measured by an aerosol monitor (TSI, DUSTTRACK II-8530-EP) for particles with sizes less than 10 µm (PM10) with a sampling frequency of 1 Hz. Meanwhile, to collect the horizontally transported sand particles during the sandstorm, the aeolian sand samplers (detailed in Dong *et al.* 2010; Wang, Gu & Zheng 2020) were deployed independently at eight heights (0.9 m, 2.5 m, 5 m, 8.5 m, 10.24 m, 14.65 m, 20.96 m and 30 m) in the wall-normal array (as shown by the green up-pointing triangles in figure 1*b*). The sand particles collected by the sand sampler (instead of the DUSTTRACK) were analysed by a commercial standard sieve analyser (MicrotracS3500) to obtain the particle size distribution at different wall-normal locations.

In addition, measurements below 0.9 m (0.03–0.5 m) were conducted in 2021 to acquire higher local mass loading than that further from the wall. The fluctuating streamwise velocity was measured by the outdoor hot-wire anemometer (ComfortSense-54T35 device from Dantec) which has a smaller probe volume (overall length of 0.3 m and shaft diameter of 0.01 m) compared with the sonic anemometer (0.6 m in length, 0.12 m in width and 0.43 m in height) and thus is more suitable for the near-wall measurement. The particle number information was acquired by the sand particle counter (SPC-91, Niigata Electric,
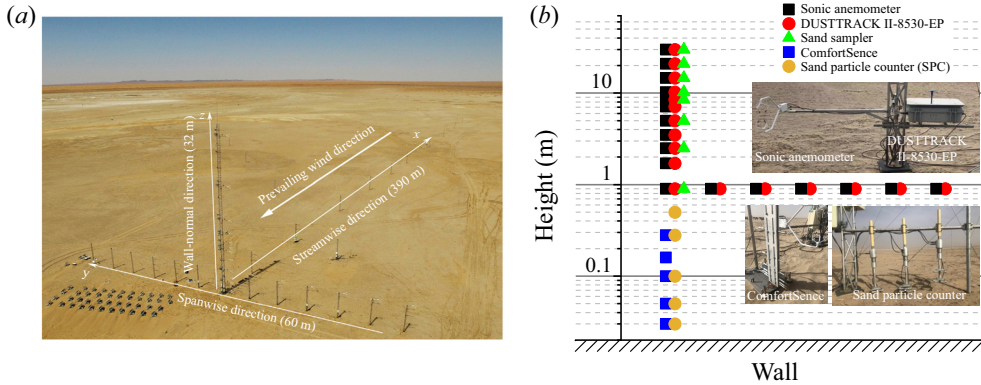
Figure 1. (*a*) Photograph of the QLOA. (*b*) Schematic of the locations of the various probes in the wall-normal and spanwise arrays that are used in this study.

previously used in Mikami 2005; Shao & Mikami 2005; Ishizuka *et al.* 2008) which covers 64 particle size groups ranging from 30 to 480 μm (a larger range of measurable particle sizes than that of DUSTTRACK) since the particles in the near-wall wind-blown sand two-phase flow are larger in diameter. The sampling frequency of both hot-wire and SPC are 1 Hz.

In the QLOA site, a soil crust is formed after rain due to the large salt content. Afterwards, the surface crust is gradually eroded, and eventually, a soft sandy surface is formed. This different degree of surface crust makes the sand concentration significantly different under the condition of a similar wind velocity. Even in the same sandstorm event, there may be significant differences in the sand concentration when a steady wind gradually develops. Taking a sandstorm with a duration of approximately 15 h from 12:00 on 16 April 2016 to 03:00 the next day as an example, figures 2(*a*) and 2(*b*) plot the corresponding streamwise velocity U and PM10 concentration C_{PM10} measured at $z = 0.9$ m. Figure 2 shows that the wind velocity increases progressively towards a plateau with a mean velocity of approximately 10 m s^{-1}. However, the PM10 concentration decreases from approximately 1.3 mg m^{-3} to near zero, while the wind velocity remains steady. This special experimental condition makes it possible to investigate the amplitude modulation under a large range of sand concentrations. It is noted that only approximately constant velocity and sand concentration data without drastic changes in mean value (as shown in the illustration in figure 2) are analysed in the present work. The observations were conducted at the QLOA site over a duration of more than 7000 h, and large amounts of particle-laden two-phase flow experimental data were obtained.

2.2. *Data processing*

Complex and uncontrollable field environmental conditions are inherent in these types of ASL measurements, thus specific selection and pre-processing are conducted on the raw data to obtain reliable datasets for the following analysis. According to the standard practice in the analysis of ASL data (Wyngaard 1992), the observational data were divided into multiple hourly time series to obtain converged statistics (Hutchins *et al.* 2012; Liu, Bo & Liang 2017*a*). The data processing includes correction for the wind direction (Wilczak, Oncley & Stage 2001), steady wind selection (judged by the non-stationary index provided in Foken *et al.* 2004), thermal stability judgment (Monin & Obukhov 1954)
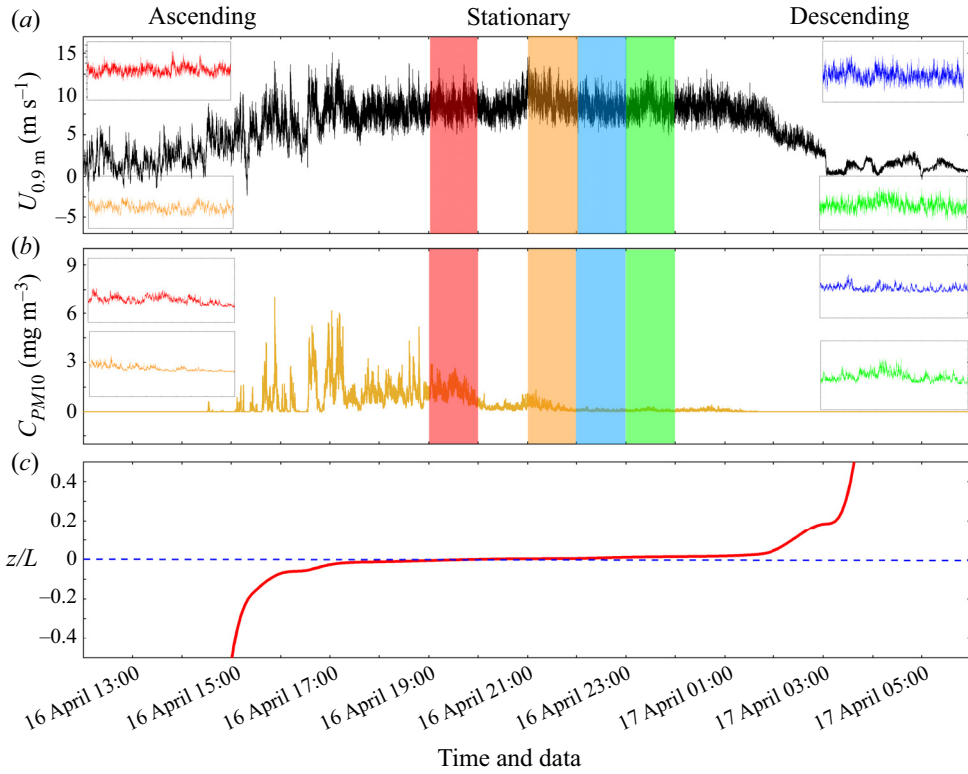
Figure 2. Streamwise velocity U (*a*), PM10 concentration C_{PM10} (*b*) and the Monin–Obukhuv stability parameter z/L (*c*) at $z = 0.9$ m during the aeolian sandstorm process from 12:00 on 16 April 2016 to 03:00 the next day. Shaded areas with different colours are time series of 4 h data that are included in table 1, and these time series are magnified in the illustrations by lines with corresponding colour.

and de-trending (Hutchins *et al.* 2012), which is consistent with Hutchins *et al.* (2012) and Wang & Zheng (2016).

The *x*-axis built into the sonic anemometer is not always along the incoming wind direction although it was installed to align with the prevailing wind direction. To acquire the actual three components of velocities, the wind direction correction is performed as

$$U = U_0 \cos(\alpha) + V_0 \sin(\alpha), \tag{2.1}$$

$$V = V_0 \cos(\alpha) - U_0 \sin(\alpha), \tag{2.2}$$

where U_0 and V_0 are the raw streamwise and spanwise velocity components in the anemometer coordinate, U and V are the actual streamwise and spanwise velocities after correction and $\alpha = \arctan(\overline{v_0}/\overline{u_0})$ is the wind direction. The vertical velocity W does not need to be corrected because the sonic anemometer was levelled during installation.

To acquire datasets with steady wind, the non-stationary index provided in Foken *et al.* (2004) is employed, which is calculated as

$$IST = |(CV_m - CV_{1h})/CV_{1h}| \times 100\,\%, \tag{2.3}$$

where $CV_m = \sum_{i=1}^{12} CV_i/12$, CV_i is the local streamwise velocity variance for every 5 min in 1 h and CV_{1h} is the overall variance of the streamwise velocity for 1 h. Following Foken *et al.* (2004), the high-quality data condition of $IST < 30\,\%$ is adopted to select the

steady wind datasets. In addition, this criterion is also applied to the sand concentration data to ensure that the duration of each dataset is chosen for stationarity based on sand concentration as well.

The Monin–Obukhuv stability parameter z/L (Stull 1988; Metzger, McKeon & Holmes 2007) is used to characterize the thermal stability, which is defined as

$$z/L = -\frac{\kappa z g \overline{w\theta}}{\bar{\theta} U_\tau^3}, \qquad (2.4)$$

where L is Obukhov length, $\kappa = 0.41$ is the Kármán constant according to the ASL study of Marusic *et al.* (2013), g is the gravitational acceleration, $\bar{\theta}$ is the average temperature, $\overline{w\theta}$ is the wall-normal heat flux obtained from the covariance between the temperature fluctuations θ and the vertical velocity fluctuations w and U_τ is the friction velocity which is estimated as $U_\tau = \sqrt{-\overline{uw}}$ at $z = 2.5$ m following Hutchins *et al.* (2012) and Li & Neuman (2012). The resulting z/L in a whole sandstorm process is shown in figure 2(*c*).

It is seen that, at the beginning of the sandstorm, z/L exhibits small negative values, indicating that the ASL is unstably stratified and buoyancy would enhance the turbulence production. As the wind speed develops to become steady, z/L reduces to values that are close to zero, indicating that the ASL is nearly neutrally stratified and thus analogous to a canonical TBL. At the decay stage of the sandstorm, z/L increases to large positive values, which suggests that the ASL is stably stratified and the turbulence is weakened. To investigate the particle effects on amplitude modulation in particle-laden flows where thermal stability effects can be considered negligible, datasets in the neutral regime should be selected. A criterion of $|z/L| \leqslant 0.04$ for a neutral stratification condition is confirmed to be applied to the particle-laden case by analysing the variations of the basic statistics and amplitude modulation coefficient vs $|z/L|$ using datasets with similar particle concentrations and different thermal stabilities (details of which are presented in the Appendix). This criterion is stricter than that of $|z/L| < 0.1$ in the existing studies (Högström 1988; Högström, Hunt & Smedman 2002; Metzger *et al.* 2007).

In addition, the de-trending manipulation proposed in Hutchins *et al.* (2012) is employed to remove the effects of the background turbulent characteristics that are directly regulated by the weather conditions and/or atmospheric motions. Due to the global nature of the weather conditions, any events registered across the entire measurement domain can be regarded as weather related. Therefore, the streamwise velocity fluctuations synchronously measured by all of the sonic anemometers over the whole array were averaged together to extract the long-term trends which are weather related (Hutchins *et al.* 2012). A low-pass filter with a cutoff wavelength of 20δ is used to obtain the broad trend. Then, the synoptic waves were subtracted from the raw data to leave just the turbulent fluctuations for further analysis.

After applying the data processing procedure, 24 h of data with similar Reynolds numbers (($3.85 \pm 1.35) \times 10^6$) and different sand concentrations spanning almost three orders of magnitude in Φ_m are subsequently analysed in this study, as listed in table 1. According to Mathis *et al.* (2009*a*) and Liu *et al.* (2019), the amplitude modulation exhibits an approximate Reynolds-number independence over three orders of magnitude in Re_τ when outer scaled with z/δ. Therefore, the outer-scaled z/δ unit was employed in the subsequent analysis to minimize the Reynolds-number effects. The ASL thickness δ at the QLOA site estimated by Wang & Zheng (2016), Liu *et al.* (2017*a*) and Liu *et al.* (2019) based on the streamwise turbulent intensity formula provided in Marusic *et al.* (2013) was $106-191$ m with an average of approximately 150 m. Moreover, the value of δ determined

No.	Date	Time	U_τ (m s^{-1})	Re_τ ($\times 10^6$)	ν ($\times 10^{-5}$ m^2 s^{-1})	z/L	Φ_m (10^{-5})
1	16 April 2016	22:00–23:00	0.42	3.9	1.62	0.01	1.23
2	16 April 2016	23:00–24:00	0.43	4.0	1.62	0.01	1.33
3	19 March 2016	05:00–06:00	0.41	3.8	1.64	0.02	1.74
4	16 April 2016	21:00–22:00	0.46	4.3	1.62	0.005	4.57
5	14 April 2016	20:00–21:00	0.42	3.6	1.73	0.01	10.78
6	14 April 2016	21:00–22:00	0.43	3.8	1.72	0.01	12.99
7	11 May 2016	16:00–17:00	0.58	5.0	1.74	−0.02	15.49
8	14 May 2016	09:00–10:00	0.54	4.8	1.68	−0.04	18.86
9	16 April 2016	19:00–20:00	0.48	4.4	1.64	0.002	19.81
10	14 April 2016	23:00–24:00	0.52	4.6	1.70	0.005	20.13
11	19 May 2016	17:00–18:00	0.59	4.9	1.81	−0.02	23.93
12	14 May 2016	11:00–12:00	0.59	5.2	1.69	−0.03	27.90
13	19 May 2016	16:00–17:00	0.59	4.8	1.83	−0.03	29.95
14	14 April 2016	22:00–23:00	0.55	4.8	1.71	0.006	31.07
15	23 May 2021	18:00–19:00	0.38	3.3	1.75	−0.003	25.1
16	14 May 2021	12:00–13:00	0.28	2.5	1.66	−0.039	52.2
17	03 May 2021	18:00–19:00	0.36	3.7	1.71	−0.024	197
18	03 May 2021	13:00–14:00	0.45	3.9	1.70	−0.035	1820
19	14 May 2021	05:00–06:00	0.39	3.4	1.74	0.01	2230
20	14 May 2021	04:00–05:00	0.40	3.5	1.74	0.01	2490
21	14 May 2021	02:00–03:00	0.43	3.7	1.75	0.01	3760
22	05 May 2021	15:00–16:00	0.58	4.8	1.79	−0.036	7900
23	29 April 2021	17:00–18:00	0.51	4.3	1.80	−0.018	9570
24	29 April 2021	16:00–17:00	0.53	4.5	1.80	−0.027	9960

Table 1. Key information relating to the datasets in the particle-laden ASL. The last column is Φ_m at the wall-normal distance $z = 0.9$ m (datasets 1–14) and $z = 0.03$ m (datasets 15–24).

by the horizontal wind speed data (> 30 m) collected by Doppler lidar in 2021 suggests that the δ under different Φ_m conditions is kept within the range of 142 ± 23 m. Thus, the ASL thickness δ is adopted as 150 m (considering that the exact choice of δ does not affect the maximum amplitude modulation coefficient between multi-scale turbulent motions and the following analysis does not involve the Reynolds-number effects). The kinematic viscosity ν was calculated by the barometric pressure and the temperature at the QLOA site (Tracy, Welch & Porter 1980).

2.3. *Two-phase flow parameters*

The last column in table 1 provides the average particle mass loading Φ_m at a wall-normal location. Here, Φ_m is estimated from the measured data of DUSTTRACK or SPC. For DUSTTRACK, the concentration of particles with sizes less than 10 µm (denoted by C_{PM10}) is measured. Therefore, to obtain the total mass loading of particles of all sizes, it is necessary to acquire the percentage of PM10 in all particles with different sizes. The particle size distribution can be obtained by analysing the collected sand particles with a commercial standard sieve analyser (MicrotracS3500), where the sand particles were collected by the aeolian sand samplers placed at different wall-normal locations. Figure 3(a) shows the resulting particle size distribution. It is seen in figure 3(a) that
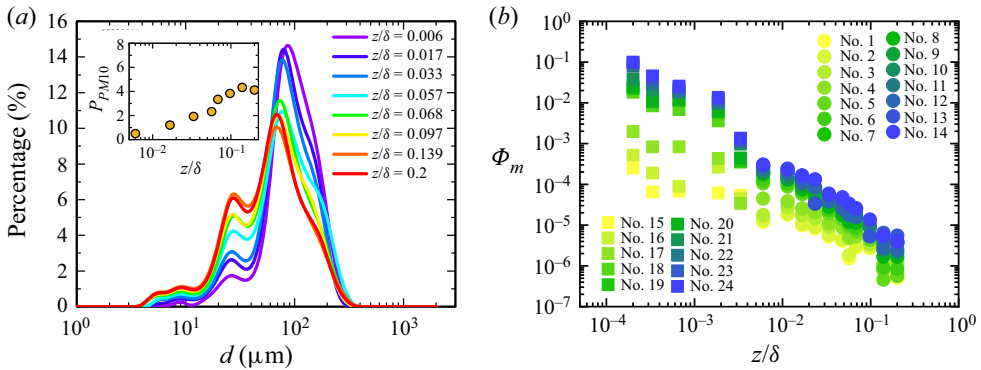
Figure 3. (*a*) Particle diameter distribution of the sand grains at different wall-normal locations, where the illustration shows the percentage of particles with diameters smaller than 10 µm. (*b*) Variation in Φ_m with the outer-scaled wall-normal distance. It is noted that 'No.' refers to the sample sets in table 1.

the diameters of sand particles present a distribution deviating slightly from a Gaussian distribution. The sand grain diameter varies from 4 to 400 µm, with the average diameters decreasing from 105 to 70 µm vs the wall-normal distance. The particle size distribution during the different events is basically the same due to the local sand source. The percentage of PM10 (denoted by P_{PM10}) at different heights is shown in the illustration in figure 3(*a*). As expected, P_{PM10} increases with z/δ. Based on P_{PM10}, Φ_m can be estimated as

$$\Phi_m = \frac{\Phi_m^{PM10}}{P_{PM10}} = \frac{\overline{C_{PM10}}}{\rho_f P_{PM10}}, \tag{2.5}$$

where Φ_m^{PM10} is the average mass loading of particles with sizes less than 10 µm (i.e. PM10 mass loading), $\rho_f \approx 1.26$ kg m^{-3} is the air density and the over bar denotes the time average.

For SPC, the large range of measurable particle sizes makes it possible to capture almost all of the near-wall sand grains. Following Shao & Mikami (2005), the particle mass flux measured by SPC is calculated as

$$q(t) = \sum_{i=1}^{64} q_i(t) = \sum_{i=1}^{64} \frac{\pi \rho_p d_i^3 N_i(t)}{6S\Delta T}, \tag{2.6}$$

where $\rho_p = 2650$ kg m^{-3} is the particle density, N_i is the number of particles of size d_i during ΔT, ΔT is time interval and $S = 5 \times 10^{-5}$ m^2 is the measurement area of the SPC. Then, based on $q(t)$, Φ_m can be estimated as

$$\Phi_m = \frac{\overline{q(t)}}{\bar{u}\rho_f}, \tag{2.7}$$

where $\bar{u}$ is the local mean velocity at the corresponding wall-normal distance.

The resulting Φ_m at different measurement heights are plotted in figure 3(*b*). It is seen that, for all of the data with different sand concentrations, Φ_m decreases progressively with the outer-scaled wall-normal distance. The variation of Φ_m with z/δ is systematic and follows an approximately linear decrease in the double logarithmic coordinates. This trend is consistent with the previously documented results of PM10 concentration vertical

957 A14-10

profile in McGowan & Clark (2008) and Panebianco, Mendez & Buschiazzo (2016) and mass flux profile in Panebianco, Buschiazzo & Zobeck (2010).

Following Li *et al.* (2021), the turbulence dissipation rate can be estimated as

$$\varepsilon = \sigma^3/l, \tag{2.8}$$

where σ is the root mean square of the streamwise velocity fluctuation and $l \propto z = \kappa z$ is based on a local scale (Tardu 2011). The characteristic length and time scale of the fluid is usually taken as the Kolmogorov scale (η, τ_η) or the integral scale (L, τ_L). The Kolmogorov length and time scale is estimated as

$$\eta = (\nu^3/\varepsilon)^{1/4}, \tag{2.9}$$

$$\tau_\eta = (\nu/\varepsilon)^{1/2}. \tag{2.10}$$

The integral time scale τ_L and the length scale L are calculated from the temporal auto-correlation function R_{uu} of the streamwise velocity fluctuations (Emes *et al.* 2019; Li *et al.* 2021), i.e.

$$R_{uu}(\tau) = \frac{\overline{u(t)u(t+\tau)}}{\sigma_t \sigma_{t+\tau}}, \tag{2.11}$$

where t is the measure time, and τ is the temporal lag. The corresponding integral time and length scale are given as

$$\tau_L = \int_0^{T_0} R_{uu}(\tau)\,\mathrm{d}\tau, \tag{2.12}$$

$$L = \bar{u}\tau_L, \tag{2.13}$$

where T_0 is the first zero-crossing point of the auto-correlation function.

The particle response time τ_p can be given as (Wang & Stock 1993)

$$\tau_p = \rho_p d_p^2/18\rho_f \nu, \tag{2.14}$$

where d_p denotes the average particle diameter at each wall-normal location. Thus, the Stokes numbers *St* based on the Kolmogorov time scale, integral time scale and viscous inner time scale are estimated as

$$St_\eta = \tau_p/\tau_\eta, \tag{2.15}$$

$$St_L = \tau_p/\tau_L, \tag{2.16}$$

$$St^+ = \tau_p u_\tau^2/\nu, \tag{2.17}$$

respectively. Moreover, the Froude number is defined as (Bernardini 2014)

$$Fr = u_\tau/\tau_p g. \tag{2.18}$$

The resulting key fluid and particle parameters related to the particle-laden flow are listed in table 2, which suggests that all cases in table 1 fall into these ranges.

2.4. *Basic statistics*

Hutchins *et al.* (2012) and Wang & Zheng (2016) confirmed that near-neutral particle-free ASL flows exhibit scaling laws that are generally representative of the canonical zero-pressure-gradient TBL, and thus can be used in studies of high-Reynolds-number

Fluid	ρ_f (kg m^{-3})	ε (m^2 s^{-3})	τ_η (10^{-2} s)	τ_L (s)	η (10^{-4} m)		L (m)	
	1.26	0.018–0.33	0.67–2.9	2.95–9.84	3.5–7.2		28.48–135.98	
Particles	ρ_p (kg m^{-3})	Scale ratio		τ_p (10^{-2} s)	*Fr*		*St*	
		d_p/η	d_p/L (10^{-7})			St_η	St_L (10^{-2})	St^+
	2650	0.1–0.3	5.15–36.8	3.13–7.57	0.38–1.92	1.08–11.29	0.32–2.56	134–1620

Table 2. Key information of fluid and particles in particle-laden flow.

wall-bounded turbulent flows, based on observational data in the Surface Layer Turbulence and Environmental Science Test (SLTEST) site and QLOA site. It is prudent to analyse particle effects on the basic statistics in particle-laden ASL flows. Figures 4(*a*)–4(*c*) show respectively the mean velocity profile, the streamwise turbulent intensity and the Reynolds shear stress for the neutral particle-laden ASL datasets used in the present work. It is seen in figure 4(*a*) that the mean velocity profiles for all of the datasets with different Φ_m follow the predicted log–linear behaviours, but there is an increasing downward shift with the Φ_m in the present ASL data compared with that for a hydraulically smooth wall ($k_s^+ < 2.25$). The downward shift trend by particles is consistent with the results in Li *et al.* (2012) and Lee & Lee (2019). Nevertheless, the equivalent sand grain roughness heights k_s^+ are approximately less than 80, which could still be in the transitionally rough regime ($2.25 \le k_x^+ \le 90$) (Ligrani & Moffat 1986) and consistent with the results for the desert surface (Metzger *et al.* 2007; Guala, Metzger & McKeon 2010; Hutchins *et al.* 2012). Figure 4(*b*) indicates that the streamwise turbulent intensity at low Φ_m is in good agreement with the existing similarity formation proposed by Marusic *et al.* (2013). As Φ_m increases, the turbulent intensity increases, which is consistent with the findings in Li & Neuman (2012), Li *et al.* (2012) and Wang *et al.* (2020). In addition, the Reynolds shear stresses in laden cases attain an approximate plateau like the unladen case in figure 4(*c*). This indicates that the 'constant stress' layer recorded in Townsend (1976) still exists in the present sand-laden flow, where the relation $-\overline{uw} = U_\tau^2$ is still satisfied. Therefore, it is suitable to estimate the friction velocity by the plateau value in the Reynolds shear stress, as is done in this study. It is for this reason that the Reynolds shear stress normalized by U_τ exhibits a plateau value of 1, which is consistent with the similarity formulation in Chauhan (2007) and Nagib & Chauhan (2008).

3. Particle effects on turbulent kinetic intensity distribution

There is a series of coherent structures with different length scales that inhabit the high-Reynolds-number wall-bounded turbulence, where the LSMs and VLSMs are dominant in the outer region. Given that the particles enhance the turbulent intensity in two-phase flow, this section aims to explore whether the influence of particles is uniform at different scale structures; that is, whether the particles change the distribution of energy of different scale motions.

To gain insight into the influence of particles on the energy distribution in different scale turbulent motions, figures 5(*a*) and 5(*b*) show the pre-multiplied energy spectra of the streamwise velocity fluctuations $k_x \Phi_{uu}/U_\tau^2$ (where $k_x = 2\pi/\lambda_x$ is the streamwise wavenumber and Φ_{uu} is the power spectral density) vs the streamwise wavenumber $k_x \delta$ at $z \approx 0.01\delta$ and $z \approx 0.02\delta$, respectively. The analysis of the pre-multiplied spectra follows
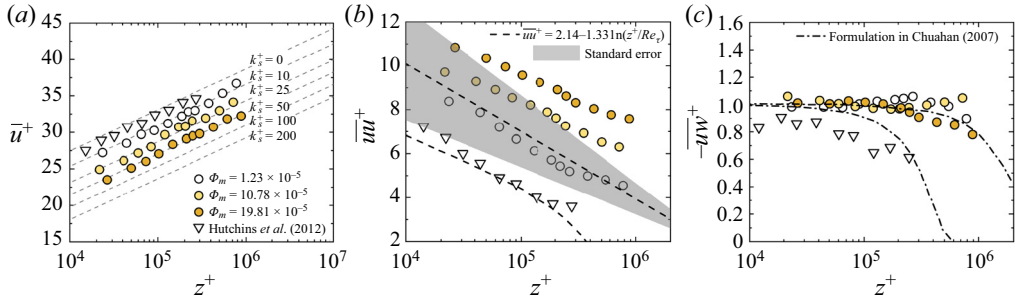
Figure 4. Variations of mean streamwise velocity profile (*a*), streamwise turbulent kinetic intensity (*b*) and Reynolds shear stress (*c*) with the inner-scaled wall-normal distance z^+. Hollow circles and yellow filled circles are the present results (nos. 1, 5, 9), hollow triangles are the result in Hutchins *et al.* (2012) at $Re_\tau = 7.7 \times 10^5$. Grey dashed lines in (*a*), $\bar{u}^+ = 1/0.41 ln(z^+) + 5.0 - \Delta\bar{u}^+$; k_s^+ is the equivalent sand grain roughness heights. Black dashed lines in (*b*) and dotted-dashed lines in (*c*) are the similarity formulations provided in Marusic *et al.* (2013) and Chuahan (2007) at the Reynolds number corresponding to the experimental data.
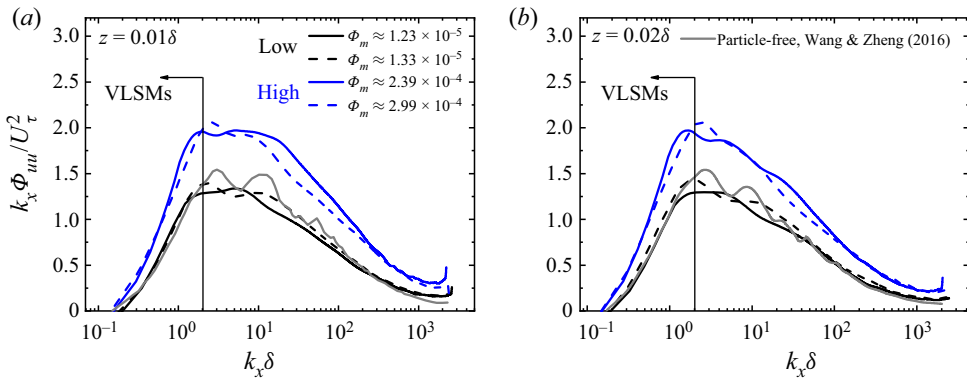
Figure 5. Pre-multiplied energy spectra of the streamwise velocity fluctuations $k_x\Phi_{uu}/U_\tau^2$ vs the streamwise wavenumber $k_x\delta$ at (*a*) $z \approx 0.01\delta$ and (*b*) $z \approx 0.02\delta$ from datasets with different particle mass loading: black lines, low Φ_m (no. 1 and no. 2); blue lines, high Φ_m (no. 11 and no. 13). The grey lines are the particle-free results in Wang & Zheng (2016).

the methods of Kim & Adrian (1999), Vallikivi, Ganapathisubramani & Smits (2015) and Wang & Zheng (2016). The results from datasets with different Φ_m are shown in figure 5 by different coloured lines for comparison, where black lines are the results for low Φ_m, blue lines are those for high Φ_m and grey lines are the particle-free flow results in Wang & Zheng (2016).

It is seen from the low Φ_m results in figure 5 that the spectral peak in the lower wavenumber region associated with the VLSMs is more distinct than the higher wavenumber peak associated with the LSMs, which suggests more dominant VLSMs in high-Reynolds-number flows than that in lower-Reynolds-number cases. This is as observed by the single-phase flow experimental results in Vallikivi *et al.* (2015), and the profiles for low Φ_m agree well with the particle-free ASL result provided in Wang & Zheng (2016). The consistency indicates that the low Φ_m data exhibit almost the same properties as are typical in the particle-free flow. In addition to a distinct peak associated with the VLSMs, the pre-multiplied energy spectra with high Φ_m in figure 5 show a significant difference from the low Φ_m results. The magnitude of the energy spectra in flows with
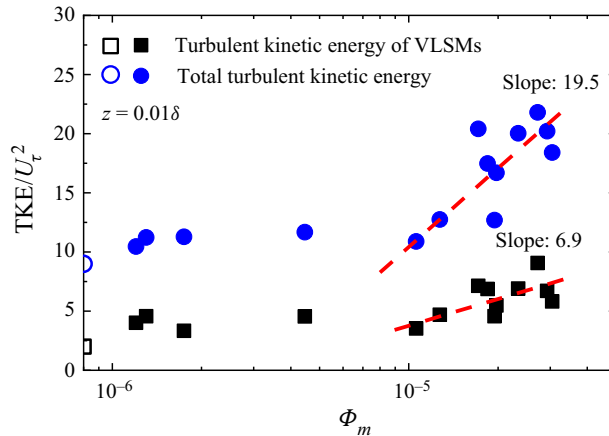
Figure 6. Changes in the turbulent kinetic energy (TKE) of the total and VLSMs with scales larger than 3δ vs Φ_m (nos. 1–14) at $z \approx 0.01\delta$. The lines are the fitting curves. The open circle and square symbols denote the particle-free ASL results in Wang & Zheng (2016).

large Φ_m is much larger than that with very small values of Φ_m, while the positions of the distinct peak remain almost unchanged. The unchanged peak position suggests that the scale of the most energetic structure does not change with the presence of particles. However, the increase of the magnitude of the energy spectra seems to be the overall uplift of the profile, with signs that the uplift is more pronounced in the higher wavenumber region than in the lower wavenumber region. This implies that the energetic signature of different scale structures is enhanced by particles in the two-phase flow, but the degree of enhancement for large-scale and small-scale components may be different.

Therefore, to further investigate the influence of particles on the kinetic energy of different scale motions, especially the VLSMs, figure 6 plots the streamwise turbulent kinetic energy of the VLSMs with length scales larger than 3δ (Guala *et al.* 2006; Balakumar & Adrian 2007) and the total streamwise turbulent kinetic energy in flows with different Φ_m. The particle-free flow results that available in Wang & Zheng (2016) are also plotted in figure 6 for comparison. It is seen in figure 6 that the streamwise turbulent kinetic energy remains almost invariant when Φ_m is small, and the previously reported values in the particle-free flow (Wang & Zheng 2016) are basically consistent with the trend. With increasing Φ_m, the turbulent kinetic energy of both the total and the VLSMs increases systematically with Φ_m, when Φ_m is larger than approximately $O(10^{-5})$. To quantify the rate of the increase with Φ_m, a log–linear equation is fitted to the experimental data (shown by dashed lines), and the slope can subsequently be obtained. The simple log–linear fit is just to quantify the growth rate, regardless of the specific functional form. It is interesting to find that the slope of the total turbulent kinetic energy increasing with Φ_m is approximately 19.5, which is much larger than the slope for the kinetic energy of VLSMs (approximately 6.9). The difference in the rate of increase indicates that, although the addition of particles in the two-phase flow enhances the turbulent kinetic energy of the VLSMs, the total turbulent kinetic energy has a more significant increase. This provides further evidence supporting that there are some differences in the influence of particles on the kinetic energy of turbulent motion at different scales. Compared with the total kinetic energy, the kinetic energy of VLSMs is less enhanced by particles, suggesting a weakened dominance of VLSMs in the two-phase flow. In addition, the variation of turbulent kinetic
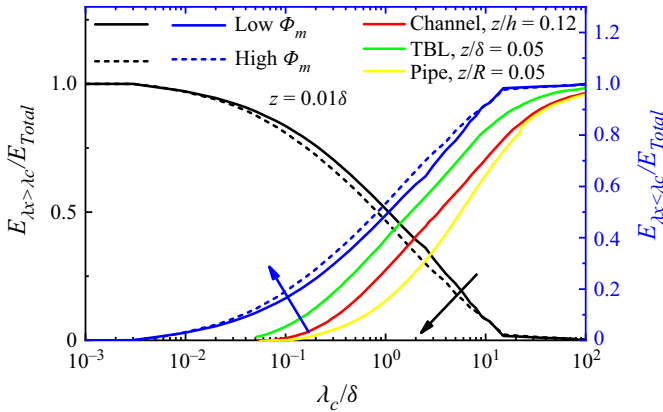
957 A14-14

Figure 7. Cumulative streamwise kinetic energy fraction associated with structures with wavelengths greater than λ_c (left vertical axis and bottom abscissa, shown by black) and less than λ_c (right vertical axis and top abscissa, shown by blue) at $z \approx 0.01\delta$. The solid lines are the average results for datasets with low Φ_m ($< 1.33 \times 10^{-5}$, nos. 1–2), and the dashed lines are those with high Φ_m ($> 1.5 \times 10^{-4}$, nos. 7–14). The red, green and yellow lines are the particle-free results in Balakumar & Adrian (2007) and Guala *et al.* (2006), respectively.

energy in particle-laden flow is different from that in Rogers & Eaton (1991), but consistent with the results in Wang *et al.* (2020), which may be related to the multiple particle sizes.

More generally, figure 7 presents the cumulative energy fraction of the streamwise velocity fluctuations as a function of wavelength (λ_c/δ). Here, $E_{\lambda_x < \lambda_c}$ is the cumulative contribution of the small-scale turbulent motion components with wavelengths from λ_c to 0 (shown in figure 7 by blue), and $E_{\lambda_x > \lambda_c}$ is the contribution from the large-scale components with wavelengths greater than λ_c (shown in figure 7 by black). The comparison of the results in particle-laden flows with large Φ_m (shown by the dashed line) and those with low Φ_m (shown by the solid line) shows that the energy fraction of the large-scale component is reduced by the addition of sand particles, while the energy fraction of the small-scale component is increased (which is more significant as compared with the particle-free TBL results in Guala *et al.* 2006; Balakumar & Adrian 2007). This phenomenon indicates that the addition of particles not only increases the energy of the VLSMs but also more significantly increases the energy of small-scale motions. That is, the particles change the distribution of energy between multi-scale turbulent motions: the energy fraction of the large-scale component is reduced, while the small-scale component is enhanced. The reduction of the energy fraction of the VLSMs in the particle-laden flow may weaken the influence on the small-scale motions, thereby reducing the amplitude modulation effect.

It is well known that the coherent structure essentially represents a three-dimensional region of a flow over which at least one fundamental flow variable (such as velocity, temperature or pressure) exhibits an obvious correlation with itself or with another variable over a large range of space and time (Robinson 1991). Moreover, the hairpin vortex packet model proposed by Kim & Adrian (1999) and Adrian *et al.* (2000) suggests that LSMs/VLSMs are created by the coherence of alignment between multiple hairpin vortices. It can be seen that the maintenance of large-scale coherent structures is closely related to the coherence between fluids. On the one hand, the disturbance of the sand particles (with gravity and large density) enhances the streamwise TKE in the particle-laden flow. On the other hand, the particle disturbance may also break the coherence of the fluctuating signals at different positions in the flow field.
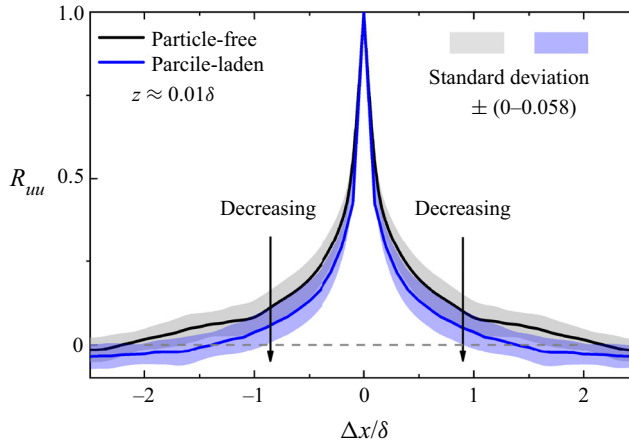
Figure 8. Time-lag streamwise velocity correlations (R_{uu}) along the streamwise direction at $z \approx 0.01\delta$. The black solid line denotes the average results for particle-free datasets available in Liu *et al.* (2019) and the blue solid line represents the average R_{uu} for datasets with $\Phi_m > 1.5 \times 10^{-4}$ (nos. 7–14). The grey and blue shaded areas are the standard deviation.

This result can be confirmed by the time-lag auto-correlation of the streamwise velocity fluctuations shown in figure 8 for both the large Φ_m case and the particle-free case. The relatively reliable average results of R_{uu} for particle-free datasets available in Liu *et al.* (2019) and particle-laden datasets with $\Phi_m > 1.5 \times 10^{-4}$ are presented in figure 8 to reduce the ASL experimental scatter. The corresponding standard deviation is approximately $\pm(0 - 0.058)$, which is shown in figure 8 by the shaded area. The abscissa in figure 8 is shown in length units by converting the temporal lead/lag (Δt) using Taylor's hypothesis of frozen turbulence ($\Delta x = \bar{u}\Delta t$, where $\bar{u}$ is the convection velocity taken as the local mean). Figure 8 shows that, at the same streamwise separation, the absolute value of the correlation coefficient R_{uu} is generally reduced in two-phase flows with large Φ_m (shown by the blue solid line) although with experimental scatter. A characteristic length scale from the time-lag auto-correlation can be extracted by a nominal threshold of R_{uu}. A small positive value is usually chosen as the threshold, such as $R_{uu} = 0.05$ (Hutchins, Hambleton & Marusic 2005), 0.1 (Dennis & Nickels 2011) and 0.4 (Tomkins & Adrian 2003). In any case, the smaller R_{uu} suggests a reduced correlation length scale. This finding indicates that sand particles weaken the coherence between fluids, and thus reduce the average scale of the coherent structures in the two-phase flow. Therefore, when the velocity fluctuations is cutoff at the same wavelength, more motions are divided into small-scale component, while fewer are divided into large-scale component. This makes the energy contained in the large-scale component decrease, while the energy contained in the small-scale component increases, as suggested in figure 7.

In summary, the analysis in this section indicates that sand particles enhance turbulence, but the degree of enhancement is different, the kinetic energy of VLSMs is less enhanced than the total kinetic energy. This changes the distribution of energy between multi-scale turbulent motions in the two-phase flow, the energy proportion of the large-scale component decreases while that of the small-scale component increases. Moreover, the addition of sand particles in the two-phase flow reduces the average scale of the coherent structures due to the weakened coherence between fluids, but hardly changes the scales of the most energetic structures.

4. Particle effects on amplitude modulation covariance

Given the change in the distribution of TKE in the particle-laden flow, especially the reduced large-scale energy proportion, it is logical then to consider their effect on the amplitude modulation of LSMs onto small scales, because the degree of amplitude modulation is closely related to the energy signature of the large-scale structures in the outer region (Mathis *et al.* 2009*a*). The amplitude modulation covariance proposed by Bernardini & Pirozzoli (2011) is an unnormalized form of the amplitude modulation, which provides a better perception of the absolute importance of the modulation effect between large- and small-scale motions. Therefore, this section explores the particle effects on the amplitude modulation covariance.

The amplitude modulation covariance is defined as the covariance between the large-scale component of the fluctuating streamwise velocity signal u_L^+ and the filtered envelope of the small-scale fluctuations $E_L(u_S^+)$. When u_L and u_S are taken from two different wall-normal locations z_1 and z_2, it presents the inter-layer (or two-point) amplitude modulation covariance, which is calculated following the method provided in Bernardini & Pirozzoli (2011) and Tong, Duan & Li (2022)

$$C_{AM}(z_1, z_2) = \overline{u_L^+(z_1)E_L(u_S^+(z_2))}, \tag{4.1}$$

where the superscript $+$ represents the inner-flow scaling normalized with the friction velocity U_τ and the kinematic viscosity ν, for example, $u^+ = u/U_\tau$, and $z^+ = zU_\tau/\nu$. The large-scale u_L^+ and the small-scale components u_S^+ of the signals are obtained by applying Fourier filters to the raw fluctuating streamwise velocity u^+ signal with a nominal cutoff wavelength. The envelope of the small-scale components $E(u_S^+)$ is extracted via the Hilbert transformation (Spark & Dutton 1972; Sreenivasan 1985) to track the changes in the amplitude of these scales. However, $E(u_S^+)$ tracks not only the large-scale modulation events due to the LSMs/VLSMs but also the small-scale variations in the carrier signal. Thus, the filtered envelope $E_L(u_S^+)$ is employed by low-pass filtering the envelope at the same cutoff as the large-scale component to describe the modulation of small-scale motions. The inter-layer amplitude modulation covariance gives a perception of the absolute importance of the modulation effect at two different wall-normal locations (z_1, z_2) (Bernardini & Pirozzoli 2011), which reflects the occurrence of a top–down interaction between LSMs in the outer region and the small-scale motions in the inner region.

The inter-layer amplitude modulation covariance extracted from low Φ_m and high Φ_m flows are plotted in figures 9(*a*) and 9(*b*), respectively. The nominal cutoff wavelength is adopted as the ASL thickness δ following Mathis *et al.* (2009*a*). It is seen from the main trend in figure 9(*a*) that the colour contour is asymmetric with respect to the diagonal line, being consistent with the high-Reynolds-number results in Bernardini & Pirozzoli (2011). The inter-layer amplitude modulation represents the effect of the outer region on the inner region, thus the region below the diagonal $(z_1 > z_2)$ is usually of most concern, and we do not discuss the results above the diagonal $(z_1 < z_2)$. Specifically, figure 9(*a*) shows an overall positive values of $C_{AM}(z_1, z_2)$ below the diagonal, and a distinct peak emerges on the bottom-right side of the map (located at approximately $z_1 \approx 0.1\delta$ and $z_2 \approx 0.02\delta$), that is, there is an off-diagonal peak as observed in Bernardini & Pirozzoli (2011). This indicates that at all of the measurement heights in the logarithmic region, the modulation is always positive when the large-scale modulating signal is located higher than the small-scale carrier signal (i.e. the top–down influence), where the LSMs near the top of the logarithmic region most significantly modulate the small scales near the mid-point of the logarithmic region. In the high Φ_m case shown in figure 9(*b*), compared with the
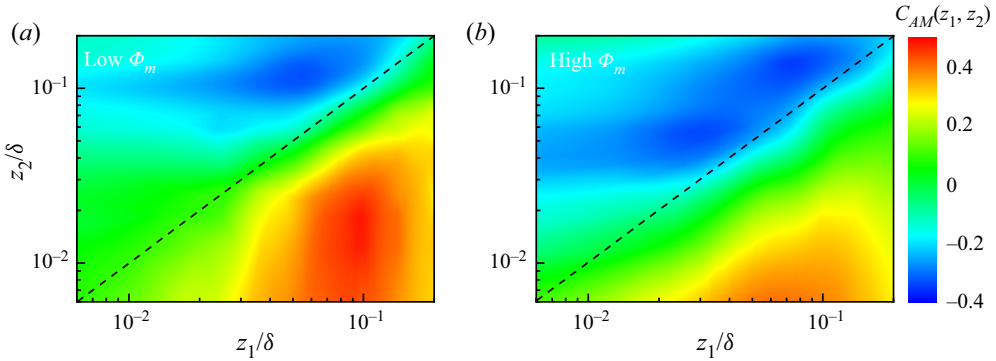
957 A14-17

Figure 9. Inter-layer amplitude modulation covariance from the large-scale turbulent motions ($\lambda_x > \delta$) at the wall-normal location z_1 onto the small-scale motions ($\lambda_x < \delta$) at z_2. (*a*) Average results for data with low Φ_m ($< 1.33 \times 10^{-5}$, nos. 1–2); (*b*) those with high Φ_m ($> 1.5 \times 10^{-4}$, nos. 7–14).

low Φ_m case, the difference is mainly reflected in two aspects: one is that the position of the off-diagonal peak slightly shifts to the lower left; the other is that the magnitude of $C_{AM}(z_1, z_2)$ decreases. The shift of the peak position indicates that the positions of the modulating signals and the carrier signals with the most significant modulation move downwards in the particle-laden flow. For the decreased $C_{AM}(z_1, z_2)$, this may be caused by the decrease in the degree of correlation, or by the decrease in the fluctuation intensities of u_L^+ and $E_L(u_S^+)$.

To analyse the amplitude modulation between multi-scale turbulent motions, two variables λ_{cL} and λ_{cS} are introduced in the decoupling procedure by Liu *et al.* (2019). Here, λ_{cL} is employed as the low-pass filter cutoff wavelength to obtain the large-scale component (wavelength $\lambda_x > \lambda_{cL}$), and λ_{cS} is adopted as the high-pass filter cutoff wavelength to obtain the small-scale component ($\lambda_x < \lambda_{cS}$). This can be given as

$$u_L^+ = u^+|(\lambda_x > \lambda_{cL}), \tag{4.2}$$

$$u_S^+ = u^+|(\lambda_x < \lambda_{cS}). \tag{4.3}$$

Correspondingly, the Hilbert transformation is applied on the small-scale component to extract the envelope, and the filtered envelope is obtained as

$$E_L(u_S^+) = E(u_S^+)|(\lambda_x > \lambda_{cL}), \tag{4.4}$$

to describe the varying amplitude of the small-scale component caused by large-scale fluctuations. Then, the amplitude modulation covariance between multi-scale turbulent motions is calculated as

$$C_{AM}(\lambda_{cL}, \lambda_{cS}) = \overline{u_L^+(\lambda_x > \lambda_{cL})E_L(u_S^+(\lambda_x < \lambda_{cS}))}, \tag{4.5}$$

where u_L and u_S are taken from the same wall-normal location.

The contours of the multi-scale amplitude modulation covariance $C_{AM}(\lambda_{cL}, \lambda_{cS})$ vs the length scales of the large-scale components ($\lambda_x > \lambda_{cL}$) and small-scale components ($\lambda_x < \lambda_{cS}$) in low and high Φ_m cases are shown in figures 10(*a*) and 10(*b*), respectively, to provide an absolute rather than a normalized value of the amplitude modulation between multi-scale turbulent motions. It can be seen in figure 10(*a*) that the peak of $C_{AM}(\lambda_{cL}, \lambda_{cS})$ can still be found at different scale turbulent motions, although the single-point modulation covariance estimated by establishing a nominal cutoff wavelength to divide the large-scale
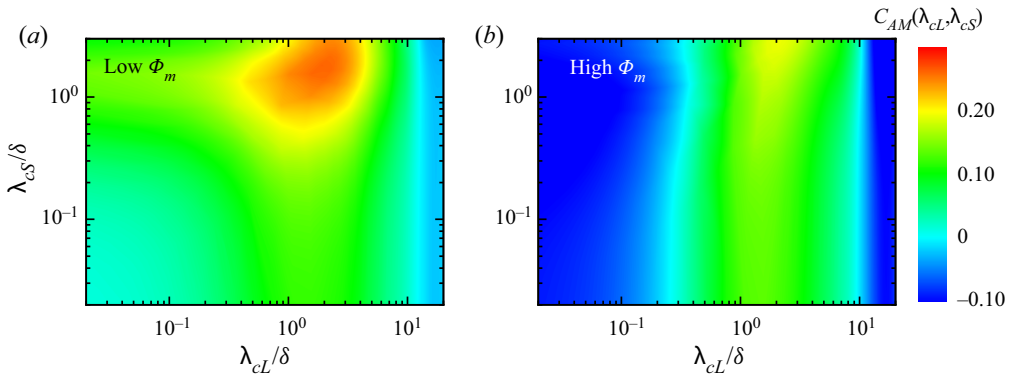
957 A14-18

Figure 10. Colour contour maps showing the variations in the amplitude modulation covariance C_{AM} $(\lambda_{cL}, \lambda_{cS})$ with the length scales of the large-scale $(\lambda_x > \lambda_{cL})$ and small-scale $(\lambda_x < \lambda_{cS})$ components at $z \approx 0.01\delta$. (*a*) Average results for data with low Φ_m ($< 1.33 \times 10^{-5}$, nos. 1−2); (*b*) those with high Φ_m ($> 1.5 \times 10^{-4}$, nos. 7−14).

and small-scale components is relatively small (as shown by the diagonal line in figure 9). The peak in the low Φ_m case is concentrated around $\lambda_{cL} \approx \lambda_{cS} \approx 2\delta$. This indicates that there is a significant modulation effect between different scales of turbulent motions at the same wall-normal location, but it only exists in some specific motions. However, the overall trend of the contour in figure 10(*a*) is quite different from the contour of multi-scale amplitude modulation coefficient provided in Liu *et al.* (2019). This may be caused by the different distributions of the fluctuation intensities of u_L^+ and $E_L(u_S^+)$ at different scales.

In addition, the comparison of high Φ_m results in figure 10(*b*) and low Φ_m results shows that the most significant difference is the attenuated magnitude of $C_{AM}(\lambda_{cL}, \lambda_{cS})$ in the high Φ_m case, making the peak value less obvious. This suggests a suppressed amplitude modulation covariance between multi-scale turbulent motions, agreeing with the damping tendency of inter-layer amplitude modulation covariance shown in figure 9.

It is noted that the amplitude modulation covariance is a dimensional quantity, which is affected by the fluctuation intensities of u_L^+ and $E_L(u_S^+)$. Therefore, to examine the distribution of their coupled fluctuation intensity for multi-scale turbulent motions and different wall-normal positions, figures 11(*a*)–11(*d*) show the contours of the root-mean-square product of u_L^+ and $E_L(u_S^+)$ in both low Φ_m and high Φ_m flows. This root-mean-square product actually represents the energetic signature of the large-scale components since $E_L(u_S^+)$ tracks the large-scale modulation events caused by u_L^+. The contours for u_L^+ and $E_L(u_S^+)$ residing at different flow layers z_1 and z_2 are shown in figures 11(*a*) and 11(*b*). Figure 11(*a*) indicates that the distribution of the root-mean-square product is quite uniform, suggesting a negligible variation of the large-scale kinetic energy with the wall-normal distance. This is consistent with the particle-free results in TBL (Balakumar & Adrian 2007), pipe (Guala *et al.* 2006) and channel (Duan *et al.* 2020) flows. The distribution of the root-mean-square product in the high Φ_m flow shown in figure 11(*b*) is similar to that in the low Φ_m case except for the increased magnitude. Therefore, the contour map of the inter-layer modulation covariance can reflect the distribution of the amplitude modulation degree in both particle-laden and unladen flows. However, the augmented energetic signature in the high Φ_m case seems to imply a reduced correlation of u_L^+ and $E_L(u_S^+)$, i.e. an attenuated degree of amplitude modulation, given the suppressed modulation covariance by particles as shown in figure 9.
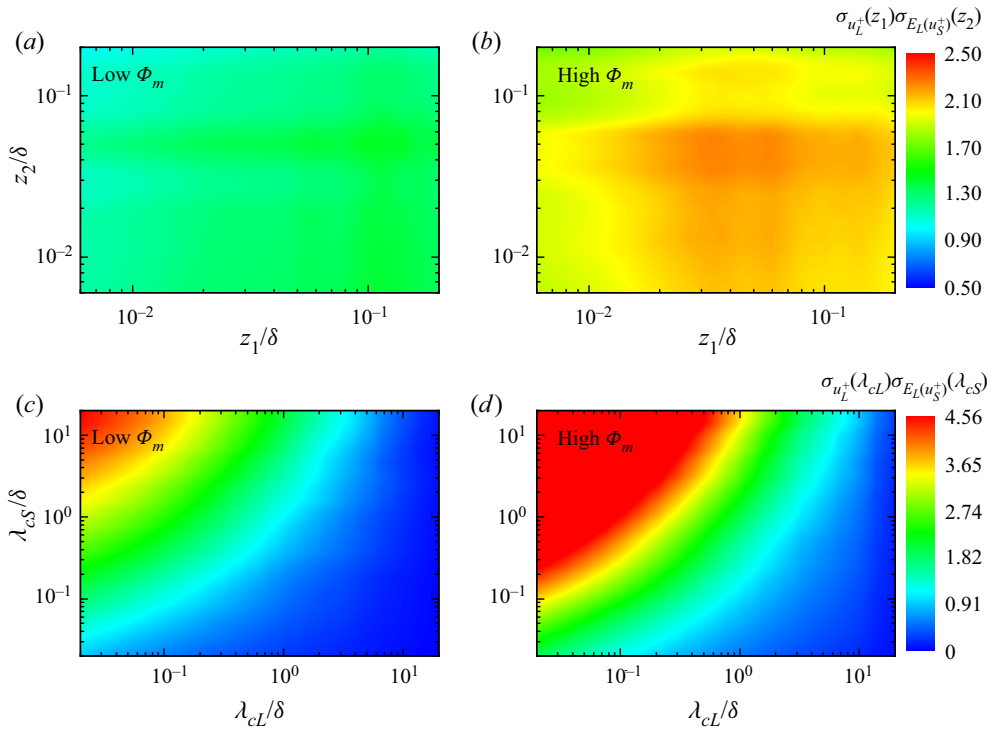
Figure 11. Contour maps of the root-mean-square product of large-scale modulating signals u_L^+ and large-scale envelope of carrier signals $E_L(u_S^+)$ in both low Φ_m (nos. 1–2) (a and c) and high Φ_m (nos. 7–14) (b and d) flows: (a) and (b) at different flow layers z_1 and z_2; (c) and (d) with different large- and small-scale cutoff wavelengths λ_{cL} and λ_{cS}.

Figures 11(c) and 11(d) show the contours for u_L^+ and $E_L(u_S^+)$ with different large- and small-scale cutoff wavelengths λ_{cL} and λ_{cS}. In both low Φ_m and high Φ_m cases, the large-scale kinetic energy significantly decreases along the bottom-right side of the map (increasing λ_{cL} and decreasing λ_{cS}). This is expected because less turbulent motion is included in u_L^+ and $E_L(u_S^+)$ as λ_{cL} increases and λ_{cS} decreases. The distribution of the large-scale energetic signature at different scales is different from the relatively uniform inter-layer energy distribution. Thus, the difference in the contours of the modulation covariance (as shown in figure 10a) and the modulation coefficient (provided in Liu *et al.* 2019) is understandable, and $C_{AM}(\lambda_{cL}, \lambda_{cS})$ cannot reflect the degree of modulation between multi-scale turbulent motions. Nevertheless, the large-scale kinetic energy is enhanced by particles for both cases of inter-layer and multi-scale root-mean-square product. This may suggest a suppressed amplitude modulation coefficient by particles given the reduced the covariance and the enhanced energy.

5. Particle effects on amplitude modulation coefficient

To explore the degree of amplitude modulation, this section presents the normalized form of amplitude modulation; that is, the amplitude modulation coefficient, a special covariance after removing the dimensional effects. The inter-layer amplitude modulation coefficient with the modulating signals and the carrier signals residing at different flow
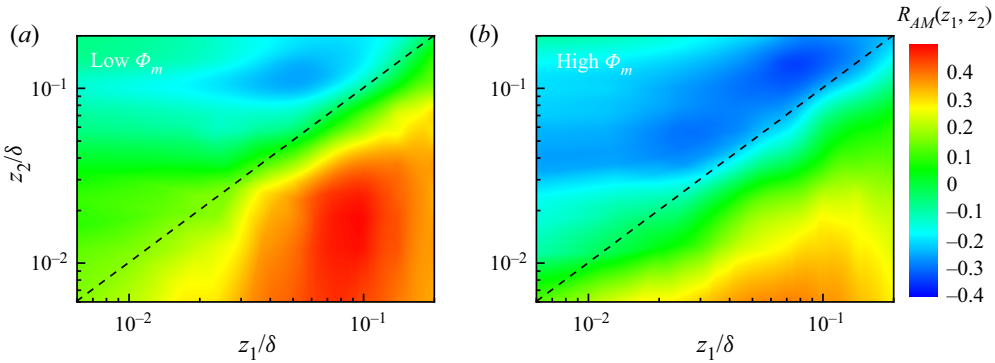
957 A14-20

Figure 12. Inter-layer amplitude modulation coefficient from the large-scale turbulent motions ($\lambda_x > \delta$) at the wall-normal location z_1 onto the small-scale motions ($\lambda_x < \delta$) at z_2. (a) Average results for data with low Φ_m ($< 1.33 \times 10^{-5}$, nos. 1–2); (b) those with high Φ_m ($> 1.5 \times 10^{-4}$, nos. 7–14).

layers and the amplitude modulation coefficient between multi-scale turbulent motions are investigated, respectively.

In an attempt to characterize and quantify the degree of the amplitude modulation, Mathis *et al.* (2009a) proposed the amplitude modulation coefficient, defined as the meaningful correlation coefficient between the large-scale modulating signals u_L^+ and the large-scale envelope of carrier signals $E_L(u_S^+)$

$$R_{AM} = \frac{\overline{u_L^+ E_L(u_S^+)}}{\sqrt{\overline{u_L^{+2}}}\sqrt{\overline{E_L(u_S^+)^2}}}, \tag{5.1}$$

that is, a normalized form of the amplitude modulation without the dimensional influence of two variables.

When u_L and u_S are taken from two different wall-normal locations z_1 and z_2, it presents the inter-layer (or two-point) amplitude modulation coefficient

$$R_{AM}(z_1, z_2) = \frac{\overline{u_L^+(z_1) E_L(u_S^+(z_2))}}{\sqrt{\overline{u_L^+(z_1)^2}}\sqrt{\overline{E_L(u_S^+(z_2))^2}}}. \tag{5.2}$$

By adopting δ as the nominal cutoff wavelength (following Mathis *et al.* 2009a), figures 12(a) and 12(b) show the inter-layer amplitude modulation coefficient from the large-scale turbulent motions ($\lambda_x > \delta$) at z_1 onto the small-scale motions ($\lambda_x < \delta$) at z_2 in low Φ_m and high Φ_m flows, respectively.

As expected, the overall trend in both figures 12(a) and 12(b) agrees well with the inter-layer covariance as shown in figure 9, the contour is asymmetric with respect to the diagonal line. Similar to figure 9, the region below the diagonal ($z_1 > z_2$) is of special concern.

Figure 12(a) shows that the inter-layer amplitude modulation coefficients $R_{AM}(z_1, z_2)$ below the diagonal exhibit very large positive values, which suggests a positive top–down modulation behaviour of the LSMs on the small-scale motions in the logarithmic region. This indicates that the near-wall small-scale fluctuations are enhanced or depressed by the positive or negative large-scale fluctuations at higher positions (Tong *et al.* 2022). In addition, there is an obvious off-diagonal peak at approximately $z_1 \approx 0.1\delta$ and $z_2 \approx$

957 A14-21

0.02δ, being consistent with the inter-layer modulation covariance as shown in figure 9(*a*). This is expected given the uniform distribution of the large-scale energetic signature at different wall-normal locations. The off-diagonal peak for $z_1 > z_2$ reflects a top–down phenomenon of the amplitude modulation, which is inherent in real turbulence signals with high Reynolds number (Bernardini & Pirozzoli 2011). The off-diagonal peak is also observed in the laboratory TBL and numerical simulation studies in Dogan *et al.* (2019), Kim *et al.* (2020) and Tong *et al.* (2022). The value of $R_{AM}(z_1, z_2)$ in the high Φ_m flow shown in figure 12(*b*) has a significant difference from the results in the low Φ_m case shown in figure 12(*a*). The magnitude of $R_{AM}(z_1, z_2)$ is reduced, and the off-diagonal peak is located at lower z_1 and z_2. This indicates that the particles produce a large damping in the degree of the amplitude modulation effect from outer LSMs on inner small-scale motions and move down the positions of the modulating signals and carrier signals corresponding to the strongest modulation effect.

To investigate the scale effects on the amplitude modulation coefficient, the amplitude modulation coefficient between multi-scale turbulent motions is calculated by substituting (4.2) and (4.4) into (5.1), which is written as

$$R_{AM}(\lambda_{cL}, \lambda_{cS}) = \frac{\overline{u^+_{L(\lambda_x > \lambda_{cL})} E_L(u^+_{S(\lambda_x < \lambda_{cS})})}}{\sqrt{\overline{u^+_{L(\lambda_x > \lambda_{cL})}}^2} \sqrt{\overline{E_L(u^+_{S(\lambda_x < \lambda_{cS})})^2}}}. \tag{5.3}$$

By comparing the amplitude modulation coefficients corresponding to different λ_{cL} and λ_{cS}, the maximum $R_{AM}(\lambda_{cL}, \lambda_{cS})$ can thus be determined. The corresponding large- and small-scale cutoff wavelengths are denoted by λ_{cL}^{PR} and λ_{cS}^{PR}, respectively; i.e.

$$\lambda_{cL}^{PR} = \lambda_{cL} | max[R_{AM}(\lambda_{cL}, \lambda_{cS})], \tag{5.4}$$

$$\lambda_{cS}^{PR} = \lambda_{cS} | max[R_{AM}(\lambda_{cL}, \lambda_{cS})], \tag{5.5}$$

representing the turbulent motions with the strongest amplitude modulation effect between them. In the following analysis, particle effects on $R_{AM}(\lambda_{cL}, \lambda_{cS})$, λ_{cL}^{PR} and λ_{cS}^{PR} are investigated in the two-phase flow.

Before analysing the scale effects on the amplitude modulation coefficient, it is prudent to check whether the $R_{AM}(\lambda_{cL}, \lambda_{cS})$ is only related to the scale ratio of the large- and small-scale cutoff wavelengths (i.e. $\lambda_{cL}/\lambda_{cS}$). Figure 13 plots the variation in $R_{AM}(\lambda_{cL}, \lambda_{cS})$ with the cutoff length scale ratio $\lambda_{cL}/\lambda_{cS}$ at $z \approx 0.01\delta$ in the particle-laden two-phase flow. The average R_{AM} for all cases with $\Phi_m > 1.5 \times 10^{-4}$ is presented in figure 13 to reduce the ASL experimental scatter. The corresponding standard deviation is approximately ± 0.06.

The different coloured lines in figure 13 represent the different lengths of small-scale motions (i.e. different λ_{cS}) that are modulated. It is seen in figure 13 that $R_{AM}(\lambda_{cL}, \lambda_{cS})$ first increases and then decreases with the scale ratio $\lambda_{cL}/\lambda_{cS}$, and this trend are qualitatively consistent for all of the different λ_{cS} cases. For a certain λ_{cS}, when λ_{cL} is small, the turbulent motions without the amplitude modulation effect are confused into the large-scale modulating signals. This leads to an underestimation of the modulation coefficient. As λ_{cL} (i.e. $\lambda_{cL}/\lambda_{cS}$) increases, these signals without modulation are gradually eliminated, increasing the modulation coefficient. Until the large-scale modulating signals are accurately extracted, $R_{AM}(\lambda_{cL}, \lambda_{cS})$ reaches the peak value. As λ_{cL} continues to increase, some of the modulating signals are missed, which also reduces the coefficient.

However, $R_{AM}(\lambda_{cL}, \lambda_{cS})$ with different λ_{cS} does not exhibit a collapse, but instead shows a significant difference. This difference suggests a non-unique $R_{AM}(\lambda_{cL}, \lambda_{cS})$ for the
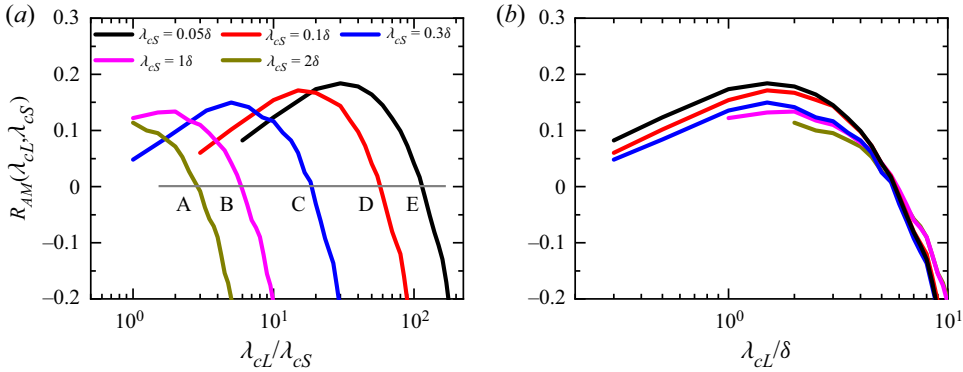
Figure 13. Variation in $R_{AM}(\lambda_{cL}, \lambda_{cS})$ with (*a*) scale ratio ($\lambda_{cL}/\lambda_{cS}$) of the large- and small-scale component cutoff wavelengths and (*b*) λ_{cL}/δ at $z \approx 0.01\delta$ in particle-laden flows with $\Phi_m > 1.5 \times 10^{-4}$ (nos. $7 - 14$).

same scale ratio, as well as a non-unique scale ratio $\lambda_{cL}/\lambda_{cS}$ for the same $R_{AM}(\lambda_{cL}, \lambda_{cS})$. Specifically, the $R_{AM}(\lambda_{cL}, \lambda_{cS})$ profiles shift for different values of λ_{cS}. An arbitrary horizontal line is plotted in figure 13(*a*), and the intersection points with the profiles are marked as A, B, C, D, E, respectively. The ratio between the abscissa of these points is equal to the reciprocal of the ratio of the corresponding λ_{cS}. This indicates that the shift is caused by the normalization of λ_{cS}, which can be confirmed by figure 13(*b*). The $R_{AM}(\lambda_{cL}, \lambda_{cS})$ profiles collapse well for different values of λ_{cS} in the abscissa of absolute scale instead of scale ratio. The peak positions are in good agreement with each other, though there are differences in the magnitude of the peak. This suggests that the LSMs with a significant modulation effect do not change with the small-scale motions being modulated, which is further supported by figure 15. Therefore, the amplitude modulation coefficient is related to the absolute scales of large- and small-scale motions, instead of their scale ratio.

To investigate the amplitude modulation effect between turbulent motions with different length scales, figure 14 shows $R_{AM}(\lambda_{cL}, \lambda_{cS})$ for varying large- and small-scale fluctuating components in particle-laden flows (shown by yellow filled circles) and compared with the results in unladen flows (open circles) provided in Liu *et al.* (2019). The error bar represents the corresponding standard deviation. The amplitude modulation coefficients from the turbulent motions with different large length scales ($\lambda_x > \lambda_{cL}$) onto the small-scale motions ($\lambda_x < 0.3\delta$, i.e. $\lambda_{cS} = 0.3\delta$) shown in figure 14(*a*) indicate that the variation in $R_{AM}(\lambda_{cL}, \lambda_{cS})$ with λ_{cL}/δ is qualitatively consistent with that in the single-phase flow. The modulation coefficient follows the trend of first increasing and then decreasing with λ_{cL}/δ, showing a distinct peak. The large-scale cutoff wavelength λ_{cL} corresponding to the peak $R_{AM}(\lambda_{cL}, \lambda_{cS})$ is λ_{cL}^{PR}, as defined in (5.4), meaning that the VLSMs with scales larger than λ_{cL}^{PR} exhibit the most significant modulation effect.

Figure 14(*b*) shows the VLSMs ($\lambda_x > \lambda_{cL}^{PR}$) modulating the turbulence motions with different short length scales ($\lambda_x < \lambda_{cS}$). It is seen in figure 14(*b*) that the trend of the modulation coefficient varying with λ_{cS}/δ also agrees with that in the particle-free flow. The value of $R_{AM}(\lambda_{cL}, \lambda_{cS})$ exhibits a gradually slowing increase as $\log(\lambda_{cS}/\delta)$ decreases and appears to level off at approximately $\lambda_{cS}/\delta = 0.08$. That is, the small-scale cutoff wavelength λ_{cS}^{PR} corresponding to the peak $R_{AM}(\lambda_{cL}, \lambda_{cS})$ is approximately 0.08δ at the outer-scaled wall-normal distance $z/\delta \approx 0.01$. This result indicates that the small-scale motions with lengths shorter than λ_{cS}^{PR} are more strongly modulated than the other scales
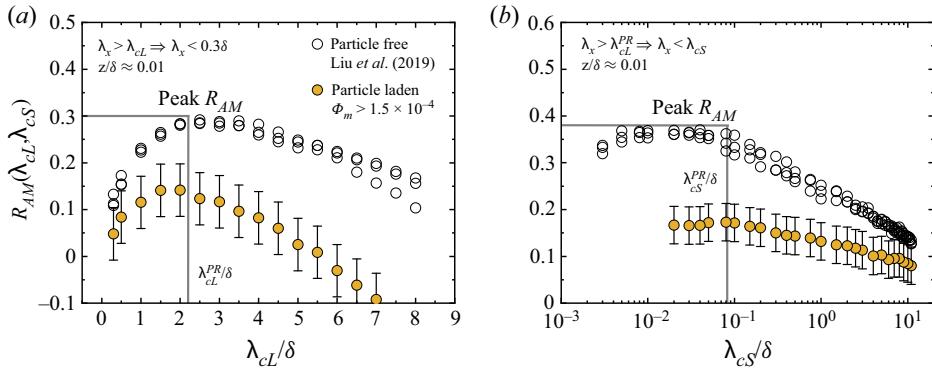
Figure 14. Comparison of $R_{AM}(\lambda_{cL}, \lambda_{cS})$ for varying large- and small-scale fluctuating components in particle-laden and particle-free flows at $z \approx 0.01\delta$. (a) $R_{AM}(\lambda_{cL}, \lambda_{cS})$ from the turbulent motions with different large length scales ($\lambda_x > \lambda_{cL}$) onto the small-scale motions ($\lambda_x < 0.3\delta$, i.e. $\lambda_{cS} = 0.3\delta$). (b) The VLSM ($\lambda_x > \lambda_{cL}^{PR}$) amplitude modulation of the motions with different short length scales ($\lambda_x < \lambda_{cS}$). The yellow filled circles are average results for datasets with $\Phi_m > 1.5 \times 10^{-4}$ (nos. 7–14). The open circles are the results in particle-free ASLs from Liu *et al.* (2019).

of motions. In addition to these qualitatively consistent results, the quantitative comparison of results in particle-laden and unladen flows suggests that the amplitude modulation coefficient decreases significantly in the particle-laden flow, while there is no drastic change in the cutoff wavelengths (i.e. λ_{cL}^{PR} and λ_{cS}^{PR}) corresponding to the maximum $R_{AM}(\lambda_{cL}, \lambda_{cS})$.

Based on the multi-scale demodulation procedure of (5.3), a two-dimensional colour contour of $R_{AM}(\lambda_{cL}, \lambda_{cS})$ as a function of both λ_{cL} and λ_{cS} in low Φ_m and high Φ_m flows is shown in figures 15(a) and 15(b) to gain a more direct insight into the amplitude modulation between the multi-scale turbulent motions. The pre-multiplied energy spectra of the streamwise velocity fluctuations $k_x \Phi_{uu}/U_\tau^2$ vs the outer-scaled wavelength λ_x/δ from the same data as the $R_{AM}(\lambda_{cL}, \lambda_{cS})$ contours are also plotted in figure 15 for comparison. The overall trend of the colour contours in figure 15 is different from the contours of multi-scale modulation covariance as shown in figure 10 due to the non-uniform distribution of the energetic signature at different scales shown in figures 11(c) and 11(d). It is seen in figure 15 that the distribution of the amplitude modulation coefficient at different scales is not random and uniform, but presents an obvious peak area around $\lambda_{cL} \approx 3\delta$ on the abscissa and on the lower part of the vertical axis (as shown by the red area). This indicates that the VLSMs with length scales larger than 3δ exhibit the most significant modulation effect on the small-scale motions at the wall-normal location of $z \approx 0.01\delta$. In addition, the peak area is vertical, which suggests that the scales of the modulating signals are constant for different scales of carrier signals. This supports the constant peak position for different λ_{cS} shown in figure 13(b). Figure 15(b) shows that the distribution of $R_{AM}(\lambda_{cL}, \lambda_{cS})$ between multi-scale motions in the high Φ_m flow is similar with that in the low Φ_m case as shown in figure 15(a) and that provided in Liu *et al.* (2019), but the magnitude of $R_{AM}(\lambda_{cL}, \lambda_{cS})$ is much smaller. The reduced $R_{AM}(\lambda_{cL}, \lambda_{cS})$ by the addition of particles is consistent with that as observed in figure 14 and the inter-layer modulation coefficient shown in figure 12. Moreover, in both low and high Φ_m cases, the peak areas of the colour contours agree well with the positions of the distinct peak in the pre-multiplied energy spectra. This indicates that the most energetic structure exhibits the strongest modulation effect.
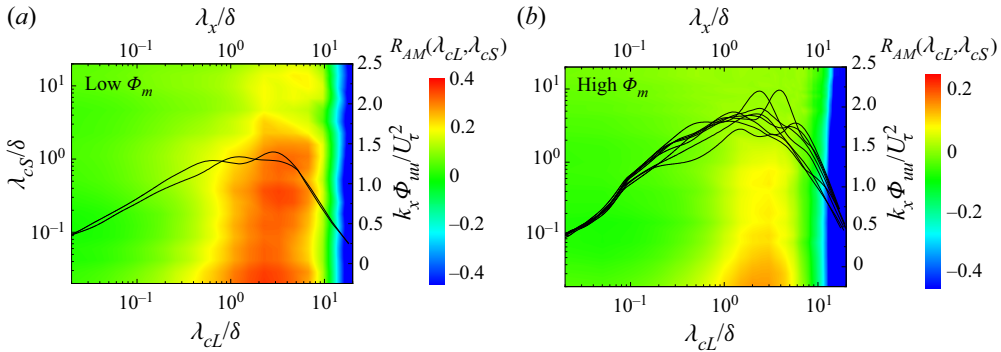
957 A14-24

Figure 15. Two-dimensional contour of $R_{AM}(\lambda_{cL}, \lambda_{cS})$ as a function of both λ_{cL} and λ_{cS} (left vertical axis and bottom abscissa) and pre-multiplied energy spectra of the streamwise velocity fluctuations $k_x \Phi_{uu}/U_\tau^2$ vs wavelength λ_x/δ (right vertical axis and top abscissa) at $z \approx 0.01\delta$ in low Φ_m (*a*) and high Φ_m (*b*) flows based on the same datasets as that in figures 9–12. Lines are the pre-multiplied energy spectra.
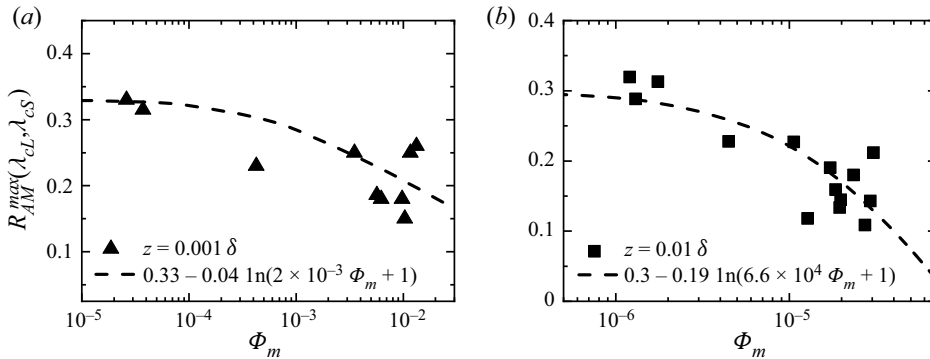

Figure 16. Variations in the amplitude modulation coefficient with the particle mass loading Φ_m at wall-normal distances of $z \approx 0.001\delta$ (nos. 15–24) (*a*) and 0.01δ (nos. 1–14) (*b*). The filled symbols are the current ASL experimental results, and the lines are the fitting curves.

To gain more information about the amplitude modulation coefficient affected by particles in two-phase flows, the analysis process in figure 15 is repeated for all of the datasets in table 1. The resulting maximum $R_{AM}(\lambda_{cL}, \lambda_{cS})$ values are summarized in figures 16(*a*) and 16(*b*) at $z \approx 0.001\delta$ and $z \approx 0.01\delta$, respectively. The abscissa is Φ_m at the corresponding wall-normal distance instead of that at $z = 0.9$ m as listed in table 1.

As expected, the amplitude modulation coefficient decreases with increasing mass loading. The variation in the maximum $R_{AM}(\lambda_{cL}, \lambda_{cS})$ with Φ_m is systematic and follows a log–linear decrease at larger Φ_m values, while $R_{AM}(\lambda_{cL}, \lambda_{cS})$ is not significantly altered at small Φ_m. This finding indicates that the interaction between multi-scale turbulent motions in the ASL is not changed in the slight wind-blown sand weather, whereas it changes drastically under aeolian sandstorm conditions. A parametric equation is fitted to the log–linear trend of the experimental data to model the variation of the maximum $R_{AM}(\lambda_{cL}, \lambda_{cS})$ with Φ_m and is given as

$$R_{AM}^{max}(\lambda_{cL}, \lambda_{cS}) = R_0 - k \ln(a\Phi_m + 1), \tag{5.6}$$

where R_0 is the amplitude modulation coefficient in a single-phase flow, k is the slope of the log–linear decrease and a is a constant. The functional form of (5.6) approaches the
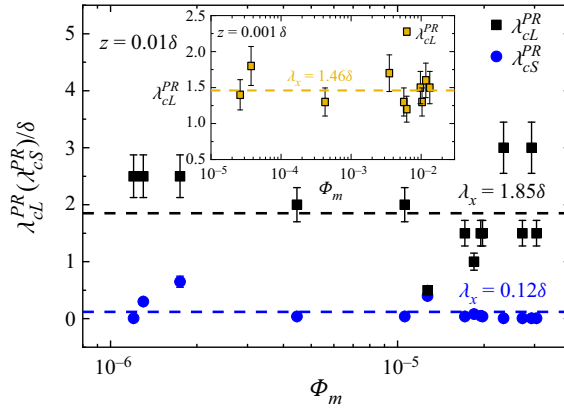
Figure 17. Large- and small-scale cutoff wavelengths (λ_{cL} and λ_{cS}) corresponding to the peak R_{AM} for varying Φ_m at different wall-normal locations of $z \approx 0.001\delta$ (nos. 15–24) and 0.01δ (nos. 1–14), respectively.

invariant value of the amplitude modulation coefficient when Φ_m is small, while it depicts the logarithmic behaviour of the modulation coefficient at a large Φ_m.

The variations in the modulation coefficient with Φ_m at different outer-scaled wall-normal distances are qualitatively consistent but with different quantitative values. The decrease in R_0 with the wall-normal distance is expected because the amplitude modulation coefficient in the single-phase flow decreases progressively with the wall-normal distance in the logarithmic region (Mathis *et al.* 2009*a*). An empirical model of the modulation coefficient in the single-phase flow that accounts for both the Reynolds number and the wall-normal distance was proposed in Liu *et al.* (2019), which provides a plausible estimation for R_0 in the logarithmic region. In addition, there are signs that the slope k increases with the wall-normal distance, which means that, farther away from the wall, the interaction between multi-scale motions is more susceptible to particles.

The resulting large- and small-scale cutoff wavelengths (λ_{cL}^{PR} and λ_{cS}^{PR}) corresponding to the maximum $R_{AM}(\lambda_{cL}, \lambda_{cS})$ at different Φ_m values at $z \approx 0.01\delta$ are plotted in figure 17, with the error bars representing the uncertainty in δ, where the illustration shows the results at $z \approx 0.001\delta$. The missing value for λ_{cS}^{PR} at $z \approx 0.001\delta$ is because of the limited sampling frequency of the ComfortSense probes. Although the experimental data are relatively scattered due to the large experimental uncertainties associated with those ASL measurements (the scatter would be smaller in a controlled laboratory experiment), the general trend of λ_{cL}^{PR} and λ_{cS}^{PR} vs Φ_m remains unchanged. At $z \approx 0.01\delta$, the average λ_{cL}^{PR} is 1.85δ, and the scatter is within $\pm 0.7\delta$, while the average λ_{cS}^{PR} is 0.12δ with a standard error of $\pm 0.07\delta$. This result is consistent with the particle-free results ($\lambda_{cL}^{PR} \approx 2.39\delta$ and $\lambda_{cS}^{PR} \approx 0.07\delta$) available in Liu *et al.* (2019) within the experimental error, providing deeper support for the invariance of λ_{cL}^{PR} and λ_{cS}^{PR} with Φ_m. The characteristic scales λ_{cL}^{PR} and λ_{cS}^{PR} represent the cutoff wavelengths of accurately extracting the modulating signals (large-scale components) and carrier signals (small-scale components) during the demodulation procedure. Therefore, their invariance suggests that the addition of sand particles may not change the turbulent motions exhibiting a significant amplitude modulation effect and that are strongly modulated; that is, the specific turbulent motions when referring to the amplitude modulation remain unchanged in the particle-laden flow. More generally, the basic mechanism of multi-scale modulation is not changing, only its magnitude, in the dilute gas-particle flow.
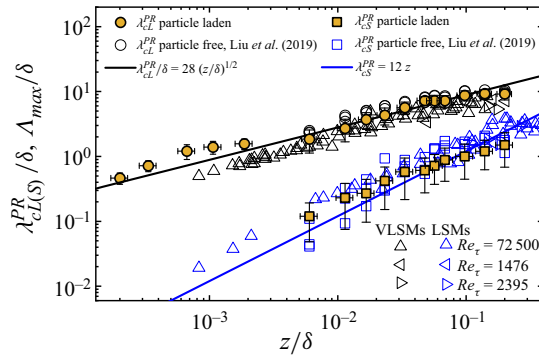
957 A14-26

Figure 18. Variations of the large- and small-scale cutoff wavelengths (λ_{cL}^{PR} and λ_{cS}^{PR}) with the outer-scaled wall-normal distance z/δ. The yellow filled symbols denote the current particle-laden ASL results for $\lambda_{cL(S)}^{PR}$ (nos. 7–24). The open circle and square symbols denote the particle-free ASL results in Liu *et al.* (2019). The open left, right and up triangle symbols are the TBL results from Balakumar & Adrian (2007) (Re_τ = 1476, 2395) and Vallikivi *et al.* (2015) (Re_τ = 72500) for wavelengths (Λ_{max}) associated with the lower wavenumber peak (VLSMs, open black symbols) and the higher wavenumber peak (LSMs, open blue symbols).

To further compare λ_{cL}^{PR} and λ_{cS}^{PR} in laden and unladen flows at all of the measurement heights in the logarithmic region and to investigate the variations of these characteristic scales with the wall-normal distance z in the particle-laden flow, figure 18 plots the average values of λ_{cL}^{PR} and λ_{cS}^{PR} for all of the datasets with $\Phi_m > 1.5 \times 10^{-4}$ and the previously documented particle-free results available in Liu *et al.* (2019). The error bars in the abscissa and vertical axis represent the corresponding the uncertainty of δ and the data standard deviation, respectively. The large- and small-scale cutoff wavelengths corresponding to the maximum modulation coefficient are associated with the lengths of the lower and the higher wavenumber peaks in the energy spectra (Liu *et al.* 2019). Therefore, the length scales of the LSMs and VLSMs associated with the higher and lower wavenumber spectral peaks that available in Balakumar & Adrian (2007) and Vallikivi *et al.* (2015) are also included in figure 18 for comparison.

It is seen from the current particle-laden ASL data in figure 18 that λ_{cL}^{PR} and λ_{cS}^{PR} increase systematically with the outer-scaled wall-normal distance z/δ. In double logarithmic coordinates, λ_{cL}^{PR} increases linearly with z/δ and follows

$$\lambda_{cL}^{PR} = 28(z\delta)^{1/2}, \tag{5.7}$$

showing a simultaneous dependence on the wall-normal distance and the ASL thickness. This dependence may be because the source of the amplitude modulation mechanism is the large δ-scaled events corresponding to the k_x^{-1} law in the turbulence spectrum (Nickels *et al.* 2005; Mathis *et al.* 2009a). The k_x^{-1} law is derived from the overlap of the low and intermediate wavenumber regions in the turbulence spectrum, where the low wavenumber range is usually scaled with the outer scale δ and the intermediate wavenumber range scales well with the local wall-normal distance z (Perry, Henbest & Chong 1986). The small-scale cutoff wavelength λ_{cS}^{PR} scales well with z as

$$\lambda_{cS}^{PR} = 12z. \tag{5.8}$$

In addition, there is an indication that λ_{cL}^{PR} and λ_{cS}^{PR} appear to level off as the wake region is approached. This is similar to the variation of the streamwise length scale of the coherent structure with the outer-scaled wall-normal distance that is observed in Tomkins & Adrian

(2003), Lee & Sung (2011) and Liu, Wang & Zheng (2017b), because the coherent structures cannot retain their coherence on evolving further away from the wall in the outer region (Marusic 2001).

By comparing the results in laden cases with those in unladen cases, figure 18 shows that λ_{cL}^{PR} and λ_{cS}^{PR} at all of the different z/δ in the logarithmic region agree well with the existing ASL results in the single-phase flow. This provides further evidence for the approximately unchanged λ_{cL}^{PR} and λ_{cS}^{PR} with Φ_m in the particle-laden flow. Moreover, λ_{cL}^{PR} and λ_{cS}^{PR} exhibit good agreement with the wavelengths of the higher and lower wavenumber spectral peaks associated with the LSMs and VLSMs, and the scaling is consistent with the trend of the corresponding wavenumbers, i.e. $k_x\delta \sim (\delta/z)^{0.5}$ and $k_x \sim z^{-1}$ (Balakumar & Adrian 2007; Vallikivi *et al.* 2015). This indicates that the multi-scale amplitude modulation is closely related to the energetic signature of the structures. In both particle-laden and unladen flows, the most energetic VLSMs with scales larger than the wavelength of the lower wavenumber spectral peak $(28(z\delta)^{1/2})$ have the most significant modulating influence on the energies (amplitudes) of the small scales shorter than the wavelength of the higher wavenumber spectral peak $(12z)$.

The accurate extraction of the modulating signals and the carrier signals during the decoupling procedure is responsible for the estimate of the amplitude modulation coefficient. Therefore, based on the above analysis, the correlation coefficient between the VLSMs with scales larger than $28(z\delta)^{1/2}$ and the filtered envelope of the small-scale motions with lengths shorter than $12z$; i.e.

$$R_{AM}^{max}(\lambda_{cL}, \lambda_{cS}) = \frac{\overline{u_{L(\lambda_x>28(z\delta)^{1/2})}^+ E_L(u_{S(\lambda_x<12z)}^+)}}{\sqrt{\overline{u_{L(\lambda_x>28(z\delta)^{1/2})}^+}^2}\sqrt{\overline{E_L(u_{S(\lambda_x<12z)}^+)^2}}}, \tag{5.9}$$

is calculated as an alternative R_{AM} to obtain the maximum amplitude modulation coefficient between multi-scale turbulent motions.

The resulting $R_{AM}^{max}(\lambda_{cL}, \lambda_{cS})$ by (5.9) at different wall-normal locations is shown in figure 19 in terms of the outer scaling, and compared with that estimated by establishing a nominal cutoff wavelength, i.e. $R_{AM}(\lambda_c = \delta)$. There is a significant difference between the modulation coefficient values obtained by these two methods in both particle-laden and unladen flows. The $R_{AM}^{max}(\lambda_{cL}, \lambda_{cS})$ value shown by blue circles is much larger than $R_{AM}(\lambda_c = \delta)$ shown by black squares, because the modulation coefficient calculated by (5.9) more specifically targets the VLSMs that dominate the amplitude modulation and the small-scale motions that are significantly subject to the modulation effect. The average increment of $R_{AM}^{max}(\lambda_{cL}, \lambda_{cS})$ relative to $R_{AM}(\lambda_c = \delta)$ at all of the measurement heights is approximately 0.13 in the particle-laden flow, while it is 0.1 in the unladen flow.

On the other hand, figure 19 shows that the modulation coefficient in the particle-laden flow (shown by yellow filled symbols) is much smaller than that in the particle-free flow (shown by open symbols), and the decrease weakens with increasing z/δ. At the low measurement height ($z \approx 0.01\delta$), the decrease in the modulation coefficient is pronounced, being reduced by approximately 0.14 due to the addition of particles. As z/δ increases, the degree of reduction tends to be negligible. At the highest measurement height ($z \approx 0.2\delta$), the modulation coefficient is only reduced by 0.05 in the particle-laden flow. The weakened decrease in the amplitude modulation coefficient with z/δ is understandable, because Φ_m decreases progressively with the wall-normal distance (as shown in figure 3b).
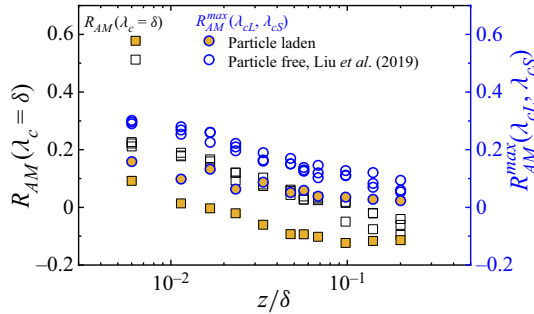
957 A14-28

Figure 19. Wall-normal profiles of the amplitude modulation coefficient in the particle-laden flow and compared with results in the particle-free flow. The yellow filled symbols denote the average results for datasets with large Φ_m (nos. 7–14 in table 1), and the open symbols are results in particle-free ASLs from Liu *et al.* (2019). The blue circles represent $R_{AM}^{max}(\lambda_{cL}, \lambda_{cS})$ calculated by (5.9) (right vertical axis) and the black squares are $R_{AM}(\lambda_c = \delta)$ estimated by establishing a nominal cutoff wavelength of δ (left vertical axis).

6. Conclusions

Large amounts of particle-laden two-phase flow data were acquired from long-term measurements of aeolian sandstorms in high-Reynolds-number ASLs at the QLOA site. Based on the experimental data with different mass loading in the near-neutral regime, the effects of sand particles on the TKE distribution and the amplitude modulation are investigated. In both particle-laden and unladen flows, at all of the measurement heights in the logarithmic region, the LSMs at higher altitudes are found to exhibit a strong positive modulation effect on the lower small-scale motions. In addition to the inter-layer modulation, a significant modulation effect that existed in some specific motions is also found for the single-point amplitude modulation, and the modulation degree is related to the absolute scales of large- and small-scale motions, instead of their scale ratio. The most energetic VLSMs with scales larger than the wavelength of the lower wavenumber spectral peak ($\sim (z\delta)^{1/2}$) have the most significant modulating influence on the energies (amplitudes) of the small scales shorter than the wavelength of the higher wavenumber spectral peak ($\sim z$). Moreover, the large-scale modulating signals do not change with the small-scale motions being modulated.

In the particle-laden flow, the length of the most energetic structure is almost constant, thus the scales of the modulating signal and carrier signal (i.e. the large- and small-scale cutoff wavelengths corresponding to the maximum modulation coefficient between multi-scale turbulent motions) is hardly affected by particles; that is, the particles do not change the turbulent motions exhibiting a significant amplitude modulation effect and that are strongly modulated. However, the addition of particles changes the distribution of energy between multi-scale turbulent motions. Compared with the total kinetic energy, the kinetic energy of VLSMs is less enhanced by particles, because the weakened coherence between fluids leads to the reduced average scale of the coherent structures. This results in the energy proportion of the large-scale component decreasing while that of the small-scale component increases. Moreover, the particles produce a large damping in the degree of the amplitude modulation and move down the positions of the modulating signals and carrier signals corresponding to the strongest inter-layer modulation. The maximum modulation coefficient (obtained by accurately extracting the modulating signals and the carrier signals during the decoupling procedure) decreases logarithmically with the particle mass loading.
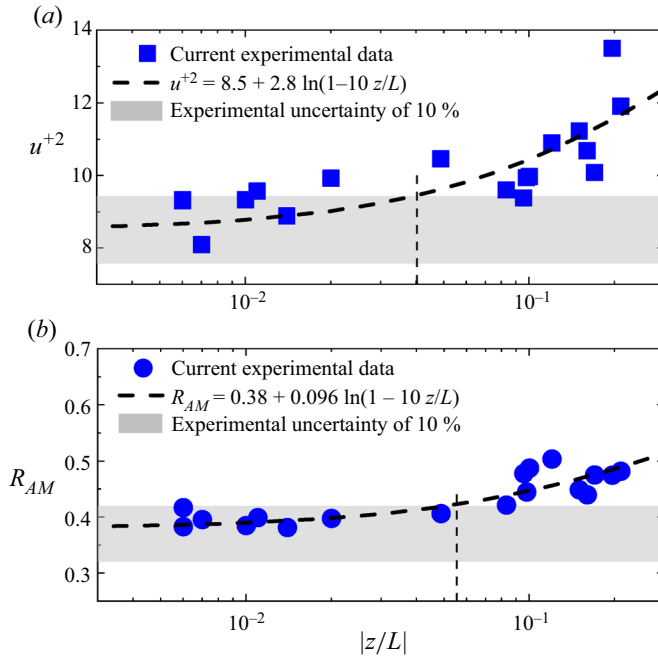
Figure 20. Variations of the streamwise turbulent intensity (*a*) and the amplitude modulation coefficient R_{AM} (*b*) with $|z/L|$. The grey shaded area denotes the experimental uncertainties according to the error analysis conducted in Metzger & Klewicki (2001), Kunkel & Marusic (2006) and Liu *et al.* (2017*a*, 2019).

No.	Date	Time	U_τ (m s^{-1})	Re_τ ($\times 10^6$)	ν ($\times 10^{-5}$ m^2 s^{-1})	z/L	Φ_m (10^{-5})
A-1	28 April 2021	14:00–15:00	0.45	3.83	1.74	−0.007	2.01
A-2	29 April 2021	11:00–12:00	0.44	3.77	1.77	−0.098	1.60
A-3	29 April 2021	13:00–14:00	0.46	3.90	1.79	−0.096	1.81
A-4	03 May 2021	15:00–16:00	0.47	4.13	1.71	−0.083	1.1
A-5	14 May 2021	02:00–03:00	0.434	3.73	1.75	0.014	1.83
A-6	14 May 2021	03:00–04:00	0.433	3.73	1.75	0.011	1.62
A-7	14 May 2021	04:00–05:00	0.402	3.46	1.74	0.01	1.20
A-8	14 May 2021	05:00–06:00	0.393	3.38	1.74	0.006	1.09
A-9	14 May 2021	06:00–07:00	0.344	3.00	1.73	0.006	0.56
A-10	14 May 2021	07:00–08:00	0.436	3.83	1.71	−0.02	2.24
A-11	24 April 2021	10:00–11:00	0.36	3.20	1.75	−0.16	0.3
A-12	24 April 2021	11:00–12:00	0.35	2.29	1.66	−0.21	0.78
A-13	24 April 2021	13:00–14:00	0.438	2.19	1.63	0.12	0.71
A-14	24 April 2021	14:00–15:00	0.381	1.89	1.63	−0.17	0.3
A-15	24 April 2021	16:00–17:00	0.38	1.87	1.66	−0.10	0.2
A-16	29 April 2021	12:00–13:00	0.46	3.90	1.78	−0.488	3.76
A-17	09 May 2021	13:00–14:00	0.38	3.11	1.87	−0.15	0.45
A-18	29 May 2021	10:00–11:00	0.325	2.62	1.87	−0.196	0.1

Table 3. Key information relating to the datasets, where the last column is Φ_m at the wall-normal distance $z = 0.03$ m.

This work studies the amplitude modulation in particle-laden ASL flows, which is a prevalent and important environmental flow. The results provide general insight into the particle effects on the inter-layer and multi-scale amplitude modulation and thus contribute to a better understanding of the particle–turbulence interaction in two-phase flow. In nature, sand grains are mixed with multiple particle sizes, which may affect the results; however, it appears that the particle-laden two-phase flow measurements in the ASL can be used as a representation of the mixed particle size behaviour.

Author ORCIDs.
Hongyou Liu https://orcid.org/0000-0002-2444-543X;
Xibo He https://orcid.org/0000-0003-0788-3566;
Xiaojing Zheng https://orcid.org/0000-0002-6845-2949.

Appendix

To discuss the issue that whether the criterion for the near-neutral stratification condition, i.e. $|z/L| < 0.1$, can be applied to the particle-laden case, another 18 sets of data with similar particle mass loading and different thermal stabilities ($z/L = -0.21 - 0.014$) are selected (listed in table 3). The variations of the basic statistics (streamwise turbulent intensity, as an example) and the amplitude modulation coefficient R_{AM} with $|z/L|$ are shown in figure 20, where the grey shaded area denotes the experimental uncertainties according to the error analysis conducted in Metzger & Klewicki (2001), Kunkel & Marusic (2006) and Liu *et al.* (2017*a*, 2019). It is seen in figure 20 that the variations of u^{+2} and R_{AM} with $|z/L|$ follow a logarithmic behaviour at high $|z/L|$ in the unstable ASL, while they are virtually unchanged within the experimental uncertainty when $|z/L| \leq 0.04$. Therefore, to investigate the variation of R_{AM} with particle mass loading in the particle-laden case under the premise of excluding the thermal stability effects, it is suitable to use the criterion of $|z/L| \leq 0.04$ for the near-neutral stratification condition.

REFERENCES

ADRIAN, R.J., MEINHART, C.D. & TOMKINS, C.D. 2000 Vortex organization in the outer region of the turbulent boundary layer. *J. Fluid Mech.* **422**, 1–54.

ANDERSON, W. 2016 Amplitude modulation of streamwise velocity fluctuations in the roughness sublayer: evidence from large-eddy simulations. *J. Fluid Mech.* **789**, 567–588.

BALACHANDAR, S. & EATON, J.K. 2010 Turbulent dispersed multiphase flow. *Annu. Rev. Fluid Mech.* **42** (1), 111–133.

BALAKUMAR, B.J. & ADRIAN, R.J. 2007 Large-and very-large-scale motions in channel and boundary-layer flows. *Phil. Trans. R. Soc. Lond.* A **365**, 665–681.

BANDYOPADHYAY, P.R. & HUSSAIN, A.K.M.F. 1984 The coupling between scales in shear flows. *Phys. Fluids* **27** (9), 2221–2228.

BERNARDINI, M. 2014 Reynolds number scaling of inertial particle statistics in turbulent channel flows. *J. Fluid Mech.* **758**, R1.

BERNARDINI, M. & PIROZZOLI, S. 2011 Inner/outer layer interactions in turbulent boundary layers: a refined measure for the large-scale amplitude modulation mechanism. *Phys. Fluids* **23** (6), 061701.

BROWN, G.L. & THOMAS, A.S. 1977 Large structure in a turbulent boundary layer. *Phys. Fluids* **20** (10), S243–S252.

CHAUHAN, K.A. 2007 Study of canonical wall-bounded turbulent flows. Thesis, Illinois Institute of Technology, Chicago.

DENNIS, D.J. 2015 Coherent structures in wall-bounded turbulence. *An. Acad. Bras. Ciênc.* **87** (2), 1161–1193.

DENNIS, D.J. & NICKELS, T.B. 2011 Experimental measurement of large-scale three-dimensional structures in a turbulent boundary layer. Part 1. Vortex packets. *J. Fluid Mech.* **673**, 180–217.

DOGAN, E., ÖRLÜ, R., GATTI, D., VINUESA, R. & SCHLATTER, P. 2019 Quantification of amplitude modulation in wall-bounded turbulence. *Fluid Dyn. Res.* **51** (1), 011408.

DONG, Z., MAN, D., LUO, W., QIAN, G., WANG, J., ZHAO, M., LIU, S., ZHU, G. & ZHU, S. 2010 Horizontal aeolian sediment flux in the minqin area, a major source of chinese dust storms. *Geomorphology* **116** (1), 58–66.

DRITSELIS, C.D. & VLACHOS, N.S. 2008 Numerical study of educed coherent structures in the near-wall region of a particle-laden channel flow. *Phys. Fluids* **20** (5), 055103.

DRITSELIS, C.D. & VLACHOS, N.S. 2011 Numerical investigation of momentum exchange between particles and coherent structures in low Re turbulent channel flow. *Phys. Fluids* **23** (2), 025103.

DUAN, Y., CHEN, Q., LI, D. & ZHONG, Q. 2020 Contributions of very large-scale motions to turbulence statistics in open channel flows. *J. Fluid Mech.* **892**, A3.

EMES, M.J., ARJOMANDI, M., KELSO, R.M. & GHANADI, F. 2019 Turbulence length scales in a low-roughness near-neutral atmospheric surface layer. *J. Turbul.* **20** (9), 545–562.

FOKEN, T., GOCKEDE, M., MAUDER, M., MAHRT, L., AMIRO, B. & MUNGER, W. 2004 Post-field data quality control. In *Handbook of Micrometeorology: A Guide for Surface Flux Measurement and Analysis* (ed. X. Lee, W. Massman & B. Law), pp. 181–208. Kluwer Academic.

GUALA, M., HOMMEMA, S.E. & ADRIAN, R.J. 2006 Large-scale and very-large-scale motions in turbulent pipe flow. *J. Fluid Mech.* **554**, 521–542.

GUALA, M., METZGER, M. & MCKEON, B.J. 2010 Intermittency in the atmospheric surface layer: Unresolved or slowly varying? *Phys. D: Nonlinear Phenom.* **239** (14), 1251–1257.

HEAD, M.R. & BANDYOPADHYAY, P. 1981 New aspects of turbulent boundary-layer structure. *J. Fluid Mech.* **107**, 297–338.

HÖGSTRÖM, U. 1988 Non-dimensional wind and temperature profiles in the atmospheric surface layer: a re-evaluation. *Boundary-Layer Meteorol.* **42**, 55–78.

HÖGSTRÖM, U., HUNT, J.C.R. & SMEDMAN, A.S. 2002 Theory and measurements for turbulence spectra and variances in the atmospheric neutral surface layer. *Boundary-Layer Meteorol.* **103** (1), 101–124.

HORST, T.W. & ONCLEY, S.P. 2006 Corrections to inertial-range power spectra measured by Csat3 and solent sonic anemometers, 1. Path-averaging errors. *Boundary-Layer Meteorol.* **119** (2), 375–395.

HUTCHINS, N., CHAUHAN, K., MARUSIC, I., MONTY, J. & KLEWICKI, J. 2012 Towards reconciling the large-scale structure of turbulent boundary layers in the atmosphere and laboratory. *Boundary-Layer Meteorol.* **145** (2), 273–306.

HUTCHINS, N., HAMBLETON, W.T. & MARUSIC, I. 2005 Inclined cross-stream stereo particle image velocimetry measurements in turbulent boundary layers. *J. Fluid Mech.* **541**, 21–54.

HUTCHINS, N. & MARUSIC, I. 2007*a* Evidence of very long meandering features in the logarithmic region of turbulent boundary layers. *J. Fluid Mech.* **579**, 1–28.

HUTCHINS, N. & MARUSIC, I. 2007*b* Large-scale influences in near-wall turbulence. *Phil. Trans. R. Soc. Lond.* A **365**, 647–664.

INOUE, M., MATHIS, R., MARUSIC, I. & PULLIN, D.I. 2012 Wall shear-stress statistics for the turbulent boundary layer by use of a predictive wall-model with LES. In *18th Australasian Fluid Mechanics Conference*. Launceston, Australia.

ISHIZUKA, M., MIKAMI, M., LEYS, J., YAMADA, Y., HEIDENREICH, S., SHAO, Y. & MCTAINSH, G.H. 2008 Effects of soil moisture and dried raindroplet crust on saltation and dust emission. *J. Geophys. Res.* **113** (D24), D24212.

JIMÉNEZ, J. & PINELLI, A. 1999 The autonomous cycle of near-wall turbulence. *J. Fluid Mech.* **389**, 335–359.

KIDANEMARIAM, A.G., CHAN-BRAUN, C., DOYCHEV, T. & UHLMANN, M. 2013 Direct numerical simulation of horizontal open channel flow with finite-size, heavy particles at low solid volume fraction. *New J. Phys.* **15** (2), 025031.

KIM, K.C. & ADRIAN, R.J. 1999 Very large-scale motion in the outer layer. *Phys. Fluids* **11** (2), 417–422.

KIM, T., BLOIS, G., BEST, J.L. & CHRISTENSEN, K.T. 2020 Experimental evidence of amplitude modulation in permeable-wall turbulence. *J. Fluid Mech.* **887**, A3.

KLINE, S.J., REYNOLDS, W.C., SCHRAUB, F.A. & RUNDSTADLER, P.W. 1967 The structure of turbulent boundary layers. *J. Fluid Mech.* **30**, 741–773.

KUNKEL, G.J. & MARUSIC, I. 2006 Study of the near-wall-turbulent region of the high-Reynolds-number boundary layer using an atmospheric flow. *J. Fluid Mech.* **548**, 375–402.

LEE, J. & LEE, C. 2019 The effect of wall-normal gravity on particle-laden near-wall turbulence. *J. Fluid Mech.* **873**, 475–507.

LEE, J.H. & SUNG, H.J. 2011 Very-large-scale motions in a turbulent boundary layer. *J. Fluid Mech.* **673**, 80–120.

LI, X.C. 2013 The influence of sandstorm on the measured results of ultrasonic anemometer. *Tech. Acoust.* **32** (2), 111–114.

LI, C., LIM, K., BERK, T., ABRAHAM, A., HEISEL, M., GUALA, M., COLETTI, F. & HONG, J. 2021 Settling and clustering of snow particles in atmospheric turbulence. *J. Fluid Mech.* **912**, A49.

LI, D., LUO, K. & FAN, J.R. 2016 Modulation of turbulence by dispersed solid particles in a spatially developing flat-plate boundary layer. *J. Fluid Mech.* **802**, 359–394.

LI, Y., MCLAUGHLIN, J.B., KONTOMARIS, K. & PORTELA, L. 2001 Numerical simulation of particle-laden turbulent channel flow. *Phys. Fluids* **13** (10), 2957–2967.

LI, B. & NEUMAN, C.M. 2012 Boundary-layer turbulence characteristics during aeolian saltation. *Geophys. Res. Lett.* **39**, L11402.

LI, J., WANG, H.F., LIU, Z.H., CHEN, S. & ZHENG, C.G. 2012 An experimental study on turbulence modification in the near-wall boundary layer of a dilute gas-particle channel flow. *Exp. Fluids* **53** (5), 1385–1403.

LIGRANI, P.M. & MOFFAT, R.J. 1986 Structure of transitionally rough and fully rough turbulent boundary layers. *J. Fluid Mech.* **162**, 69–98.

LIU, H.Y., BO, T.L. & LIANG, Y.R. 2017*a* The variation of large-scale structure inclination angles in high Reynolds number atmospheric surface layers. *Phys. Fluids* **29** (3), 035104.

LIU, H.Y., WANG, G.H. & ZHENG, X.J. 2017*b* Spatial length scales of large-scale structures in atmospheric surface layers. *Phys. Rev. Fluids* **2**, 064606.

LIU, H.Y., WANG, G.H. & ZHENG, X.J. 2019 Amplitude modulation between multi-scale turbulent motions in high-Reynolds-number atmospheric surface layers. *J. Fluid Mech.* **861**, 585–607.

LUHAR, M., SHARMA, A.S. & MCKEON, B.J. 2014 On the structure and origin of pressure fluctuations in wall turbulence: predictions based on the resolvent analysis. *J. Fluid Mech.* **751**, 38–70.

MARUSIC, I. 2001 On the role of large-scale structures in wall turbulence. *Phys. Fluids* **13** (3), 735–743.

MARUSIC, I., MATHIS, R. & HUTCHINS, N. 2010*b* Predictive model for wall-bounded turbulent flow. *Science* **329** (5988), 193–196.

MARUSIC, I., MATHIS, R. & HUTCHINS, N. 2011 A wall-shear stress predictive model. In *13th European Turbulence Conference (ETC13)*, Journal of Physics: Conference Series, vol. 318, p. 012003. IOP Publishing.

MARUSIC, I., MCKEON, B.J., MONKEWITZ, P.A., NAGIB, H.M., SMITS, A.J. & SREENIVASAN, K.R. 2010*a* Wall-bounded turbulent flows at high Reynolds numbers: recent advances and key issues. *Phys. Fluids* **22** (6), 065103.

MARUSIC, I., MONTY, J.P., HULTMARK, M. & SMITS, A.J. 2013 On the logarithmic region in wall turbulence. *J. Fluid Mech.* **716**, R3.

MATHAI, V., LOHSE, D. & SUN, C. 2020 Bubbly and buoyant particle-laden turbulent flows. *Annu. Rev. Condens. Matter Phys.* **11** (1), 529–559.

MATHIS, R., HUTCHINS, N. & MARUSIC, I. 2009*a* Large-scale amplitude modulation of the small-scale structures in turbulent boundary layers. *J. Fluid Mech.* **628**, 311–337.

MATHIS, R., HUTCHINS, N. & MARUSIC, I. 2011 A predictive inner–outer model for streamwise turbulence statistics in wall-bounded flows. *J. Fluid Mech.* **681**, 537–566.

MATHIS, R., MARUSIC, I., CHERNYSHENKO, S.I. & HUTCHINS, N. 2013 Estimating wall-shear-stress fluctuations given an outer region input. *J. Fluid Mech.* **715**, 163–180.

MATHIS, R., MONTY, J.P., HUTCHINS, N. & MARUSIC, I. 2009*b* Comparison of large-scale amplitude modulation in turbulent boundary layers, pipes, and channel flows. *Phys. Fluids* **21** (11), 111703.

MATINPOUR, H., BENNETT, S., ATKINSON, J. & GUALA, M. 2019 Modulation of time-mean and turbulent flow by suspended sediment. *Phys. Rev. Fluids* **4**, 074605.

MCGOWAN, H.A. & CLARK, A. 2008 A vertical profile of PM10 dust concentrations measured during a regional dust event identified by MODIS Terra, Western Queensland, Australia. *J. Geophys. Res.* **113** (F2), F02S03.

METZGER, M.M. & KLEWICKI, J.C. 2001 A comparative study of near-wall turbulence in high and low Reynolds number boundary layers. *Phys. Fluids* **13** (3), 692–701.

METZGER, M., MCKEON, B.J. & HOLMES, H. 2007 The near-neutral atmospheric surface layer: turbulence and non-stationarity. *Phil. Trans. R. Soc. Lond.* A **365**, 859–876.

MIKAMI, M. 2005 Measurement of saltation process over gobi and sand dunes in the Taklimakan desert, China, with newly developed sand particle counter. *J. Geophys. Res.* **110** (D18), D18S02.

MONIN, A. & OBUKHOV, S. 1954 Basic laws of turbulent mixing in the surface layer of the atmosphere. *Tr. Akad. Nauk. SSSR Geophiz. Inst.* **24** (151), 163–187.

NADEEM, M., LEE, J.H., LEE, J. & SUNG, H.J. 2015 Turbulent boundary layers over sparsely-spaced rod-roughened walls. *Intl J. Heat Fluid Flow* **56**, 16–27.

NAGIB, H.M. & CHAUHAN, K.A. 2008 Variations of von Kármán coefficient in canonical flows. *Phys. Fluids* **20** (10), 101518.

NICKELS, T.B., MARUSIC, I., HAFEZ, S. & CHONG, M.S. 2005 Evidence of the k_1^{-1} law in a high-Reynolds-number turbulent boundary layer. *Phys. Rev. Lett.* **95**, 074501.

PANEBIANCO, J.E., BUSCHIAZZO, D.E. & ZOBECK, T.M. 2010 Comparison of different mass transport calculation methods for wind erosion quantification purposes. *Earth Surf. Process. Landf.* **35** (13), 1548–1555.

PANEBIANCO, J.E., MENDEZ, M.J. & BUSCHIAZZO, D.E. 2016 PM10 emission, sandblasting efficiency and vertical entrainment during successive wind-erosion events: a wind-tunnel approach. *Boundary-Layer Meteorol.* **161** (2), 335–353.

PATHIKONDA, G. & CHRISTENSEN, K.T. 2017 Inner–outer interactions in a turbulent boundary layer overlying complex roughness. *Phys. Rev. Fluids* **2** (4), 044603.

PERRY, A.E., HENBEST, S.M. & CHONG, M.S. 1986 A theoretical and experimental study of wall turbulence. *J. Fluid Mech.* **165**, 163–199.

PETERSEN, A.J., BAKER, L. & COLETTI, F. 2019 Experimental study of inertial particles clustering and settling in homogeneous turbulence. *J. Fluid Mech.* **864**, 925–970.

PICANO, F., BREUGEM, W.-P. & BRANDT, L. 2015 Turbulent channel flow of dense suspensions of neutrally buoyant spheres. *J. Fluid Mech.* **764**, 463–487.

PORTELA, L.M. & OLIEMANS, R.V. 2003 Eulerian-lagrangian DNS/LES of particle-turbulence interactions in wall-bounded flows. *Intl J. Numer. Meth. Flow* **43** (9), 1045–1065.

RAJAGOPALAN, S. & ANTONIA, R.A. 1980 Interaction between large and small scale motions in a two-dimensional turbulent duct flow. *Phys. Fluids* **23** (6), 1101–1110.

ROBINSON, S.K. 1991 Coherent motions in the turbulent boundary layer. *Annu. Rev. Fluid Mech.* **23**, 601–639.

ROGERS, C.B. & EATON, J.K. 1991 The effect of small particles on fluid turbulence in a flat-plate, turbulent boundary layer in air. *Phys. Fluids* A*: Fluid Dyn.* **3** (5), 928–937.

SALESKY, S.T. & ANDERSON, W. 2018 Buoyancy effects on large-scale motions in convective atmospheric boundary layers: implications for modulation of near-wall processes. *J. Fluid Mech.* **856**, 135–168.

SCHOPPA, W. & HUSSAIN, F. 2002 Coherent structure generation in near-wall turbulence. *J. Fluid Mech.* **453**, 57–108.

SHAO, Y. & MIKAMI, M. 2005 Heterogeneous saltation: theory, observation and comparison. *Boundary-Layer Meteorol.* **115** (3), 359–379.

SMITH, C.R. 1984 A synthesized model of the near-wall behavior in turbulent boundary layers. In *Proceedings of the 8th Symposium on Turbulence*. University of Missouri-Rolla.

SPARK, E.H. & DUTTON, J.A. 1972 Phase angle considerations in the modeling of intermittent turbulence. *J. Atmos. Sci.* **29** (2), 300–303.

SQUIRE, D.T., BAARS, W.J., HUTCHINS, N. & MARUSIC, I. 2016 Inner–outer interactions in rough-wall turbulence. *J. Turbul.* **17** (12), 1159–1178.

SREENIVASAN, K.R. 1985 On the fine-scale intermittency of turbulence. *J. Fluid Mech.* **151**, 81–103.

STULL, R.B. 1988 *An Introduction to Boundary Layer Meteorology*. Springer.

TALLURU, K.M., BAIDYA, R., HUTCHINS, N. & MARUSIC, I. 2014 Amplitude modulation of all three velocity components in turbulent boundary layers. *J. Fluid Mech.* **746**, R1.

TARDU, S.F. 2011 *Statistical Approach to Wall Turbulence*. John Wiley & Sons, Ltd.

TAY, G.F., KUHN, D.C. & TACHIE, M.F. 2015 Effects of sedimenting particles on the turbulence structure in a horizontal channel flow. *Phys. Fluids* **27** (2), 025106.

THEODORSEN, T. 1952 Mechanism of turbulence. In *Proceedings of the Second Midwestern Conference on Fluid Mechanics*, pp. 1–19. Ohio State University.

TOMKINS, C.D. & ADRIAN, R.J. 2003 Spanwise structure and scale growth in turbulent boundary layers. *J. Fluid Mech.* **490**, 37–74.

TONG, F., DUAN, J. & LI, X. 2022 Characteristics of reattached boundary layer in shock wave and turbulent boundary layer interaction. *Chin. J. Aeronaut.* **35** (6), 172–185.

TOSCHI, F. & BODENSCHATZ, E. 2009 Lagrangian properties of particles in turbulence. *Annu. Rev. Fluid Mech.* **41** (1), 375–404.

TOWNSEND, A.A. 1976 *The Structure of Turbulent Shear Flow*, 2nd edn. Cambridge University Press.

TRACY, C.R., WELCH, W.R. & PORTER, W.P. 1980 Properties of air: a manual for use in biophysical ecology. *Tech. Rep.* 1. Department of Zoology, University of Wisconsin, Madison.

Tsuji, Y., Marusic, I. & Johansson, A.V. 2016 Amplitude modulation of pressure in turbulent boundary layer. *Intl J. Heat Fluid Flow* **61**, 2–11.

Vallikivi, M., Ganapathisubramani, B. & Smits, A.J. 2015 Spectral scaling in boundary layers and pipes at very high Reynolds numbers. *J. Fluid Mech.* **771**, 303–326.

Wang, H. & Gao, Q. 2021 A study of inner-outer interactions in turbulent channel flows by interactive pod. *Theor. Appl. Mech. Lett.* **11** (1), 100222.

Wang, G.H., Gu, H.H. & Zheng, X.J. 2020 Large scale structures of turbulent flows in the atmospheric surface layer with and without sand. *Phys. Fluids* **32** (10), 106604.

Wang, G. & Richter, D.H. 2019 Two mechanisms of modulation of very-large-scale motions by inertial particles in open channel flow. *J. Fluid Mech.* **868**, 538–559.

Wang, L.P. & Stock, D.E. 1993 Dispersion of heavy particles by turbulent motion. *J. Atmos. Sci.* **50** (13), 1897–1913.

Wang, G.H. & Zheng, X.J. 2016 Very large scale motions in the atmospheric surface layer: a field investigation. *J. Fluid Mech.* **802**, 464–489.

Wilczak, J.M., Oncley, S.P. & Stage, S.A. 2001 Sonic anemometer tilt correction algorithms. *Boundary-Layer Meteorol.* **99** (1), 127–150.

Wyngaard, J.C. 1992 Atmospheric turbulence. *Annu. Rev. Fluid Mech.* **24** (1), 205–234.

Yao, Y.C., Huang, W.X. & Xu, C.X. 2018 Amplitude modulation and extreme events in turbulent channel flow. *Acta Mech. Sin.* **34**, 1–9.

Zhao, L.H., Andersson, H.I. & Gillissen, J.J.J. 2010 Turbulence modulation and drag reduction by spherical particles. *Phys. Fluids* **22** (8), 081702.